CAN A RADAR EMULATOR BE USED TO IDENTIFY SIMULATED PRE-TORNADIC SMALL-SCALE VORTICITY?

By

Noah Harley

A thesis submitted in partial fulfillment of the requirements for the degree of

Bachelor of Arts

Houghton University

May 2025

Signature of Author……..
Department of Physics
May 5, 2025

……..
Dr. Mark Yuly
Professor of Physics

……..
Dr. Brandon Hoffman
Professor of Physics

CAN A RADAR EMULATOR BE USED TO IDENTIFY SIMULATED PRE-TORNADIC SMALL-SCALE VORTICITY?

By

Noah Harley

Submitted to the Department of Physics
on May 5, 2025 in partial fulfillment of the
requirement for the degree of
Bachelor of Arts

Abstract

Tornadoes are largely unpredictable severe weather events that are chaotic in nature. Much of this unpredictability stems from a lack of specific knowledge regarding the process of tornadogenesis. This thesis describes a proposed investigation of pre-tornadic, surface-based, small-scale vorticity present in the high-resolution Cloud Model 1 numerical convective simulation of the May 24, 2011, El Reno tornadic supercell. The radar emulator RSim will be used to sample the simulated storm using different radar wavelengths, range resolutions, azimuthal resolutions, beamwidths, and other parameters similar to real-world radar sampling strategies. This will potentially allow scanning radar parameters to be optimized, enabling future field campaigns to test for the presence of this pre-tornadic phenomenon. The collaboration would include researchers from the Ohio State University, the University of Wisconsin-Madison, and the University of Oklahoma.

Thesis Supervisor: Dr. Mark Yuly
Title: Professor of Physics

TABLE OF CONTENTS

TABLE OF FIGURES

Chapter 1

HISTORICAL AND MODERN APPROACHES TO TORANDO RESEARCH

1.1. Overview

Recent research [1] has found that human-induced climate change has the potential to move and expand the regions typically associated with tornadic activity. Another study [2] put the current false-alarm tornado warning rate at a staggering 75%. Findings such as these have continued to motivate the meteorological community to study the process of tornado formation; also called tornadogenesis. Tornadoes can form in many types of systems, from lines of strong thunderstorms to tropical storms and hurricanes to isolated supercells. Supercells are highly structured, singular systems of intense, sustained convection (upward movement of warm air), and are responsible for statistics [3] such as 97% of fatalities, 96% of injuries, and 92% of damage relating to tornadoes. This skewed tornadic impact towards supercells therefore motivates the proposed research focus on supercellular tornadic activity. While widely studied, there lies the potential for scientific breakthroughs relating to the surface-based winds that converge prior to the formation of the main tornadic vortex. This introduction covers general information about tornadoes and the history of tornado research, recent discoveries about the surface-based winds during tornadogenesis, numerical simulations and radar emulators as they pertain to the research proposed, and motivation for the proposed study.

1.2. Tornadoes: Characteristics and Climatology

A tornado can be defined [4] simply as a series of intense, columnar masses of whirling air (vortices) that make contact with the ground and are capable of inflicting damage. The vortex is sometimes visible as a funnel cloud if the internal pressure deficit is low enough to cause the condensation of water vapor and the subsequent formation of cloud particles. Tornadoes can also be encased in precipitation and may be deemed “rain wrapped.” While most tornadoes last about 10 minutes [4], they have been recorded to last between a few seconds to over an hour. Their diameter is typically near 200 m [4]; however, this diameter can be as

small as 10 m or as large as 2 km [4]. Wind speeds associated with tornadoes have been recorded to be between 20-140 m/s [4].

The first official attempt to rate the strength of a tornado was by Theodore T. Fujita in 1970 with his “F-scale” [5]. The F-scale estimated wind speed based on the nature and extent of the damage inflicted by the tornadic winds, with severity from 0 to 5. The scale began to break down over the next few decades as the relationship between wind speed and damage had not been thoroughly investigated under controlled conditions. In 2007, the National Weather Service (NWS) adopted the Enhanced Fujita (EF) Scale [6]. This new scale kept the 0 to 5 ratings but changed the range of wind speeds at which structures “failed” for certain degrees of damage and specific damage indicators. The EF Scale is now also based on the quality of the building or object’s construction. This scale is continually being updated to reflect advances in structural engineering and wind-speed estimations, with the most recent revision [6] being recommended in 2022.

Damage from tornadoes has five main origins [4]: pressure differences from wind, transient responses to wind gusts, airflow interaction with structures resulting in varying aerodynamic effects, flying debris, and structures tipping and rolling.

There also exist a wide variety of other tornado-like phenomena [4]. Waterspouts, tornadoes that form over water, are typically weaker than land-based tornadoes. Dust devils, fire whirls, and steam devils all have vortex-like shapes, and typically result from surface heating.

While most tornadoes occur in the United States, they have been documented to occur all over the world. Within the United States, the central (Great Plains) and southeast states experience the most tornadic activity per year [4]. This region is a bullseye for tornado formation due to the combination of warm, moist air from the Gulf of Mexico to the south, cold-air injections from Canada to the north, and complex storm systems transitioning from the Rocky Mountain terrain to the flat Great Plains terrain to the west. The states along the Gulf of Mexico experience their highest amount of tornadic activity in the late winter, and the core of the activity moves north and west into the Great Plains and Midwest in the spring.

Tornadoes can form at any time of day or night but are most common in the Great Plains during the late afternoon due to the climax of the diurnal heating cycle.

1.3. History of Tornado Research

Compared to other fields of science, official meteorological observations were not taken routinely in the United States until the late 1800s. The individual collection of data on weather phenomena evolved into local and regional forecasting, which gave rise to national weather agencies. On the research side, some of those same weather reports evolved into tornado-based research, which then split into supercell and tornadogenesis research fields.

1.3.1. Early Observations

The collection of meteorological observations in the United States officially began around 1870 with the US Army Signal Corps' creation [7] of a specified meteorology division: the Weather Bureau. In the next eight years, the number of operational field stations collecting meteorological data increased from 24 to 284, and the reports expanded to include temperature, wind velocity and direction, barometric pressure, amount of cloud cover, and humidity. In 1877, John Park Finley enlisted and began collecting tornado reports [8]. He was assigned to testing the feasibility of forecasting tornadoes in 1882 and quickly enlisted a spotter network to widen his dataset [9]. Soon thereafter in 1884, Finley developed the first list of "rules" [10] for forecasting a tornado. For the next year and a half, he issued experimental tornado predictions regularly, but suspicious statistical counting of mis-forecasted events led some to not trust Finley's findings [7].

A series of changes in jurisdiction and office locations ensued in the following years, disrupting Finley's work [7]. His tornado forecasting plan was halted indefinitely in when the 1887 *Report of the Chief Signal Officer* [11] claimed that predictions of tornadoes would cause more harm than that resulting from a tornado itself. However, the ongoing civilian-military feud over weather forecasting and research control was likely the primary catalyst of the downfall of Finley's project. The sentiment of this report was reinforced [12] in 1890 by Professor Henry A. Hazen. He concluded that tornado forecastability was too difficult at the time and that prediction should be left for future meteorologists. These statements were further reinforced in 1915 [13] and 1934 [14] after the Weather Bureau Stations Regulations

of 1905 [15] officially prohibited the forecasting of tornadoes. By 1940, little to no progress [7] had been made in the forecasting of tornadoes due to the fear of public panic and the forecasting ban.

1.3.2. Early Forecasting and New Establishments

Tornado forecasting made significant progress in 1948 with the first successful tornado forecast [16] by Ernest J Fawbush and Robert C Miller. On March 20th, 1948, the Tinker Air Force Base Weather Station in Oklahoma City, Oklahoma, was struck by a damaging tornado that caused $10 million in damages and injured numerous workers. Fawbush and Miller, forecasters at the station, spent the next four days analyzing upper-air and surface weather charts created prior to the tornado and from past outbreaks. They identified similarities and listed parameters sufficient for tornadic outbreaks, discovering that their main difficulty was projecting the parameters in space and time to predict a threat area with lead-time and a reasonable degree of confidence. On March 25th, the two observed storms approaching their region and noted that the weather charts closely resembled those from five days earlier, when the March 20th tornado struck. At 2:50 pm, Fawbush and Miller issued the first official tornado forecast for the area surrounding the base, and at 6 pm the forecast came to pass. The base was struck by another strong tornado, but the forecast allowed for preparations that resulted in $4 million less in damages and no injuries.

The next ten years were marked by a rapid evolution of meteorological forecasting and the establishment of research/forecast centers. In 1951, the Severe Weather Warning Center (SWWC) was established [17] at Tinker Base under the direction of Miller and Fawbush. The Weather Bureau-Army-Navy (WBAN) Analysis Center (also called the Severe Weather Unit) was established by the Weather Bureau in 1953. Later that year, the Severe Weather Unit was renamed the Severe Local Storm Warning Service (SELS), followed by the joining of SWWC and SELS in Kansas City, Missouri. The Tornado Research Airplane Project (TRAP) [18] was formed by SELS later in 1956, with the goal of using aircraft to investigate the humidity and temperature structure of air in tornado forecast regions. The Severe Local Storms Synopsis product [17] was initiated in 1958, which released daily convective outlooks. In 1964, the National Severe Storms Laboratory was formed in Norman Oklahoma,

and it continues to be a leading laboratory in research regarding severe weather. Several research experiments were conducted in the following decades through SELS and the Weather Bureau, and in 1963 the SELS Center received [19] its first computer. The Techniques Development Unit (associated with SELS) was created in 1976, directed by Joseph T. Schaefer, with the promise of conducting applied severe weather research and developing computer-based techniques for improving forecasts of severe weather. In 1995, the SELS unit in Kansas City was renamed the Storm Prediction Center, which today produces long- and short-range convective outlooks for the continental United States.

1.3.3. Early Tornado Research

The history of tornado research was documented in detail in a paper [19] by Joseph Galway, and the following description outlines some key aspects. Tornado research through the Weather Bureau began around 1950 with Dr. Morris Tepper of the Weather Bureau's Scientific Services Division. Tepper believed that accelerations of air along a cold front traveling along a warm sector inversion as gravitational waves (horizontally-traveling transverse waves in the atmosphere with vertical polarization) were the cause of squall lines (lines of severe thunderstorms). This idea became known as the "pressure jump line" tornado mechanism, and it led to the creation of the Tornado Project. Initially a small number of stations reporting environmental conditions such as temperature, humidity, wind, precipitation, and pressure around Washington D.C., the Tornado Project turned into a 3-year endeavor spanning multiple states that collected data on hundreds of tornadoes. The Tornado Project's first season in 1951 did not amount to much due to a lack of tornadoes to study. In its second season in 1952, the project was renamed the Tornado and Squall Line Project, and 143 tornadoes were reported. Evidence was found that something other than the intersecting pressure jumps was the driving mechanism behind most tornadic development. The Tornado Project's third and final season in 1953 (renamed the Severe Local Storms Research Unit) saw additional observational networks in 10 states, with 67 regular reporting stations and 128 other stations. In this season, tornadoes were found to be associated with a pressure couplet—the first record of this nature.

In March of 1952, WBAN [19] added a twice daily analysis of upper-air data into their tornado and severe thunderstorm forecasts, which allowed them to calculate the "potential instability" of the environment. In 1960, the Weather Bureau created a collaboration program with the Federal Aviation Agency, the National Aeronautics and Space Administration, the U.S. Air Force, and the U.S. Navy, in which multiple plane missions would be conducted in and around squall lines and thunderstorms. This program was called the National Severe Storms Project, and it effectively took over TRAP.

1.3.4. Supercell and Tornadogenesis Research

The 1940s saw the earliest modern supercell research when surveillance meteorological radar detected echoes with anomalous motion [20]. These echoes were first deemed "hooks" by Edgar van Tassel in 1955 [21], just two years after Donald A. Staggs of the Illinois State Water Survey documented the first reflectivity image of a hook-shaped radar echo [22], shown in Figure 1. Described as downward extensions of the rear side of a heightened region of reflectivity, hook echoes are typically oriented perpendicular to the storm's motion [23].

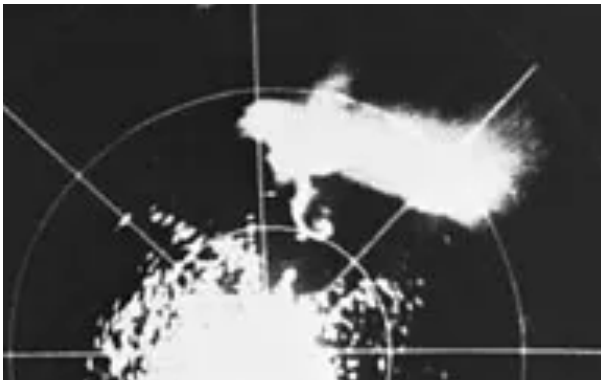

Figure 1. First radar reflectivity image of a tornadic supercell's hook echo. This image of a tornadic supercell was taken on April 9, 1953, near Champaign, IL. Figure taken from Ref. [22].

Since then, correlations between supercell and hook echo formation and pre-storm environment variables have improved forecasting storms and investigating the theories behind them [24]. It became increasingly evident during the 1970s that storm rotation and tornadoes are directly associated with strong horizontal shear (changes in wind speed or direction with respect to position) zones and hook echoes [25]. The 1970s also saw the

introduction of multi-Doppler radar observations alongside high-speed computer simulations [26]. These advancements allowed for comparisons between simulated properties of supercells and real-world observations. The next few decades included numerous field experiments and the development of many simulations, all of which resulted in furthering scientists' understanding of the fluid dynamics of supercells [27]. Supercells that are associated with heightened probabilities of producing tornadoes have been better understood in recent years, as diagrams like Figure 2 have been developed that detail the wind in and around supercells, as well as the storm's main components.

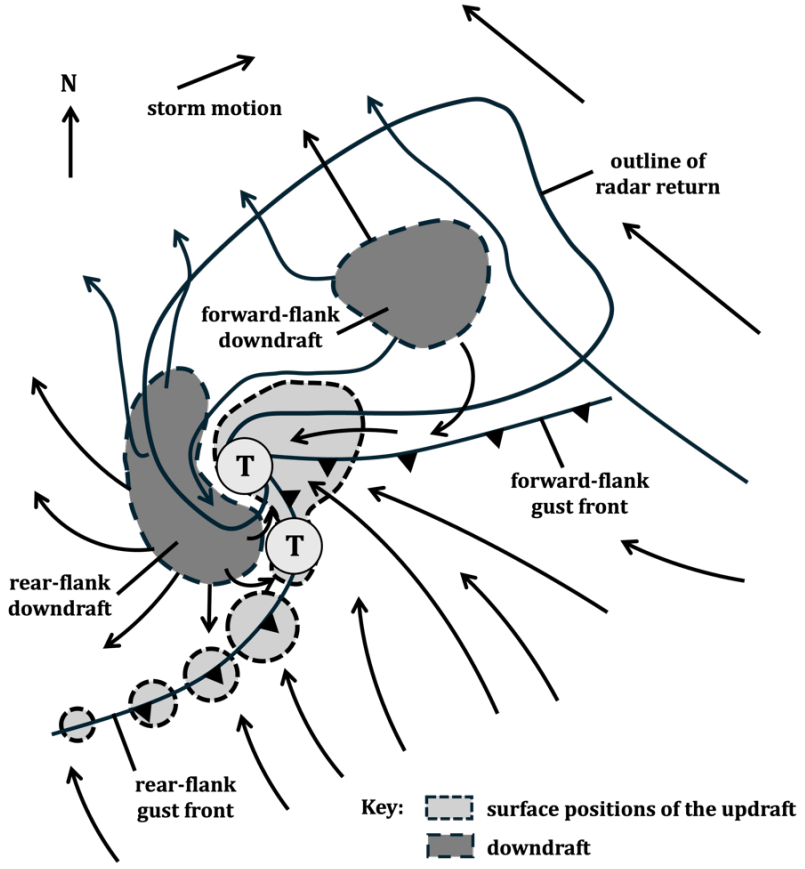

Figure 2. Surface plan view of a tornadic supercell. The shape outlined by the solid black line encompasses what the radar visualizes, with the shaded regions symbolizing regions of rising or falling air. Each arrow designates the flow of air at different points in and around the supercell. The encircled "T" symbols represent the typical tornadic regions. Figure adapted from Ref. [70].

As more research has been conducted, several important terms have developed regarding tornadic supercells; with many of these identified in Figure 2. The rear-flank downdraft (RFD) is a region of dry air that descends on the back side of a supercell. Consensus was gained with respect to the RFD's involvement [23] in tornadic supercells in the late 1970s and early 1980s. The hook echo of a supercell was found [28] to represent a precipitation band accompanied by the RFD and subsequent outflow of air, partially surrounding a region of inflow and updraft (air moving towards the storm and up). Another region of downward-moving air in a mature supercell is the forward-flank downdraft (FFD). Forming downwind of the updraft (with respect to the storm's relative motion), the FFD [29] results from the central updraft's downstream movement of condensate. These downdrafts form gust fronts that move with the storm: the RFD being associated with the rear-flank gust front and FFD the forward-flank gust front. Typically, the most significant tornadoes develop at the center of mesocyclone (defined in the northern hemisphere as a cyclonically rotating column of air), and touch down near the updraft-downdraft interface [29], as shown by the upper encircled "T" in Figure 2. A secondary region of heightened tornado production sometimes exists along the RFD's gust front.

The first substantiated tornadogenesis theory [29] was formulated in 1979 by Leslie Lemon and Charles Doswell from the Techniques Development Unit. They updated the reigning conceptual model of a supercell [20], created by Keith Browning in 1964, to include the RFD. Lemon and Doswell's theory [29] postulated that tilting and stretching of the tornadic vortex was the primary source of vertical vorticity. The two also ruled out the belief of the presence of shear vortices along the forward-flank gust front aiding in tornadogenesis. Their theory also proposed that the primary tornadic vortex forms aloft and then descends with the RFD.

Vorticity is an integral part of understanding tornadogenesis and thus warrants a brief description. Best described as a measure of the rotation of a fluid at a specific point, vorticity is calculated [30] by

$$\vec{\zeta} = \vec{\nabla} \times \vec{v}\,, \tag{1}$$

with velocity vector $\vec{v}$. The resulting vorticity has units of inverse seconds and is commonly represented by the variable zeta in meteorology. Due to cyclonic rotation being

counterclockwise in the Northern Hemisphere, the vorticity vector typically points in the upward ($\hat{k}$) direction. Vorticity is typically associated with wind shear: a change in wind speed or direction with height. This wind shear can cause horizontal vorticity: rotation of air around an axis parallel to the ground. This horizontal vorticity's axis of rotation can then be rotated/tilted [31] into the vertical and turned into vertical vorticity: rotation along an axis perpendicular to the ground.

One of the more modern studies on tornadogenesis was conducted by Paul Markowski and Yevette Richardson in 2014 [32]. This study attempted to quantify the effects of cold-pool buoyancy—the idea that a mass of cold air sinks due to its increased density—and low-level wind shear on tornadogenesis using simulated "pseudo-storms." The simulations suggested that stronger mesocyclones closer to the surface are more likely to form in environments with significant streamwise vorticity (strong low-level wind shear). The study also highlighted the role of misalignments in atmospheric temperature and pressure gradients in generating downdrafts, as well as the importance of horizontal vorticity in the development of near-surface vertical vorticity. The two noted that they did not include moist processes such as hydrometeors (liquid or solid water particles in the atmosphere) or latent heating (energy flow upon phase change) in their simulations, as they wanted to reduce the degrees of freedom.

1.3.5. Near-Surface Vertical Vorticity

Identifying the processes generating near-surface vertical vorticity directly prior to the formation of a tornado has been a more recent endeavor undertaken by meteorologists. One of the earliest, most prominent studies on near-surface vertical vorticity was conducted by Robert Davies-Jones and Harold Brooks in 1993 [33]. The two performed idealized simulations and investigated how horizontal vorticity could be reoriented into vertical vorticity through the interaction with a supercell's downdraft. Another mechanism was identified by Robert Trapp and Morris Weisman in 2003 [34], which discussed tornadogenesis in quasi-linear-convective systems (a line of strong thunderstorms, typically oriented north to south, forming along a cold front) and the importance of amplification and stretching of the vertical vortex by the updraft. In 2017, Richard Rotunno and his partners

used Lagrangian analyses—which focus on the properties of air parcels as they move through space rather than focusing on a fixed point (Eulerian)—on an idealized-supercell simulation to investigate near-ground vorticity [35]. Their study supported Davies-Jones' and Brook's mechanism of vortex tilting [33] and suggested that the downdraft is at least partially responsible for the generation of near-surface horizontal vorticity through imbalances in temperature and pressure gradients (baroclinic mechanisms). The two provided further evidence that the tilting and stretching of horizontal vorticity into the vertical is responsible for the production of significant vertical vorticity, and therefore only horizontal vorticity is needed near the surface for tornadogenesis.

It is equally important to acknowledge the limitations of this research, as they expose numerous opportunities for further exploration of the process of tornadogenesis. The simulations discussed in the previous paragraph largely ignore the impacts of friction, which is problematic as many recently performed studies indicate friction's vital role in this process. In 2016, Brett Roberts and his colleagues conducted research [36] on surface drag's role in tornadogenesis via an idealized supercell simulation. They identified three potential roles of surface friction in tornadogenesis, with the first being environmental generation of near-surface horizontal vorticity. Surface drag creates a large amount of low-level environmental wind shear, which translates into large horizontal vorticity. This vorticity can then be tilted into the vertical through the mechanisms described previously [35] and then stretched, producing a low-level mesocyclone. Second, they found that near-surface horizontal vorticity can be generated by surface drag within and around the convective storm, adding to the first effect. Lastly, surface drag was identified to possibly be involved in the enhancement of low-level convergence (the converging and subsequent rising of air at a point in space) underneath the mesocyclone. Shortly thereafter, Roberts was involved in two additional studies on the effects of surface drag [37, 38], both of which supported the previous findings.

1.4. Convective Numerical Simulations

Numerical convective storm models are used for meteorological research in many ways, including to depict and study the behaviors of storm features, carry out case studies of

observed events, and study the response of a storm to changes in the environment [39]. Numerical modeling requires solving systems of equations describing numerous atmospheric variables on scales ranging from a few meters to hundreds of kilometers. In the earliest days of solving these systems, simplifications were made that were motivated by limitations imposed by computer memory, data storage capacity, and speed, as well as the desire to only focus on "key" dynamical processes. Cloud Model 1, the numerical model used in this proposal, is a recent development built on decades of prior research.

1.4.1. Early Simulations

In 1963, Yoshimitsu Ogura of the Massachusetts Institution of Technology investigated and described numerous numerical simulations conducted in years prior, creating the first severe local storms monograph [40]. Gravity waves, which are caused by changes in gravitational forces, and sound waves, which are rapid pressure changes in the air, were removed from the preexisting nonhydrostatic (not assuming hydrostatic balance between pressure gradient forces and gravity) equations. The model was anelastic, signifying the lack of an elastic energy term in the kinetic-potential energy equation. Following this research, succeeding models were split into either anelastic or compressible ($\vec{\nabla} \cdot \vec{V} \neq 0$) models.

Terry Clark designed a three-dimensional weather model [41] in 1976 to simulate air flow over irregular terrain. This model's primary purpose was to focus on accurately describing surface boundary conditions: specifically, those dealing with wave drag. Wave drag is a force that acts against the movement of air in the atmosphere caused by the generation and dissipation of gravity waves when air flows over uneven terrain. Important for atmospheric models attempting to simulate real-world properties, evidence of adherence to the conservation of energy was provided. Then in 1978, Richard Anthes and Thomas Warner developed a hydrostatic mesoscale meteorological model [42] capable of simulating large flows on scales down to 5 km and making real data forecasts on the synoptic (large) scale.

The 1978 hydrostatic model [42] was advanced in 1992 by Jimy Dudhia of The Pennsylvania State University into a new version of the Penn State—NCAR Mesoscale Model (PSU/NCAR) [43] with nonhydrostatic capability and higher resolution grids. This model vastly improved the capabilities associated with numerical convective simulations, as it took ideas from

numerous previous studies and models. It incorporated an improved representation of the planetary boundary layer (the lowest 1-2 km of the atmosphere) from a high-resolution, one-dimensional, moist planetary boundary layer model developed in 1982 by Dalin Zhang and Anthes [44]. A more accurate surface radiation budget (the balance of incoming and outgoing radiation on the surface) was added based on results from Stanley Benjamin and Toby Carlson's 1986 experiment [45] in which they used a version of Anthes and Warner's 1978 model [42] coupled with Zhang and Anthes' 1982 work [44] on the planetary boundary later to study the effects of surface heating on the evolution of severe storm environments. Another addition to Dudhia's model [43] was an explicit moisture scheme based on a two-dimensional numerical model [46] created by Eirh-Yu Hsie et al. in 1984 used to simulate the formation of weather fronts to understand how heat released by water vapor affects the circulation around those fronts. This model included ways to more accurately calculate cloud formation and rain—vital components for small-scale convective simulations. Also important to Dudhia's model was the addition of several cumulus parameterization schemes based on modifications made to the PSU/NCAR model in 1986 by Zhang and Michael Fritsch [47], which enabled the simulation of smaller scale convection (2-20 km in size).

A three-dimensional model [48], created by Gregory Tripoli, focused on simulating the interactions between different types of atmospheric motions in convective weather systems was also introduced in 1992. This model was designed to conserve kinetic energy and enstrophy in three dimensions, while minimizing errors from numerical calculations. Enstrophy, related to vorticity, quantifies the total rotational motion of a fluid, and is related to the rate of energy loss in a vortex due to friction. Louis Wicker and William Skamarock created a new forward-in-time splitting method called the Second-Order Runge-Kutta scheme in 1998 [49], which greatly aided in the integration of elastic equations. Their method was then used successfully in the Collaborative Model for Multiscale Atmospheric Simulation [50] —a full-physics nonhydrostatic model.

1.4.2. Cloud Model 1 Overview

From 2000 to 2002, George Bryan borrowed techniques and ideas from numerical models described previously and developed the First-Generation Pennsylvania State University

National Center for Atmospheric Research Cloud Model (CM1) [51]. CM1 is a three-dimensional, non-linear, nonhydrostatic, time-dependent numerical model [52] designed to study small-scale processes that occur in the Earth's atmosphere [53]. While its design is like those of Tripoli 1992 [48] and Wicker and Skamarock 1998 [49], its creation was revolutionary because unlike the aforementioned models, CM1 includes phase changes of cloud water and water vapor [51]. CM1 conserves energy and mass better than other modern cloud models and is designed for very large domain simulations with high resolution, so the code can be applied to very large problems as the model has comparatively little memory overhead [53]. It is highly effective for a wide range of problems across various scales due to its versatility in handing different equation sets and applications, such as compressible, incompressible, or anelastic flows. Additionally, it outperforms other cloud models like the Advanced Research WRF and the ARPS in terms of speed and memory efficiency (RAM).

Cloud Model 1 provides details of the convective potential of the environment, the likelihood of organized atmospheric phenomena such as squall lines and supercells, and other information such as the trajectory and severity of the storms simulated [54]. These attributes allow CM1 to be utilized for many studies requiring numerical simulations of convection. In 2021, the model was used for the analysis of a supercell that spawned large hail and a tornado at the Vienna International Airport in 2017 [55]. The research focused on the triggering factors of the supercell and subsequent tornado formation. In 2021, CM1 was used in a study [56] of high-shear, low-CAPE (convective available potential energy) supercells. It was also utilized that year as the simulation in a study [57] that analyzed winds, reflectivity, and streamwise vorticity currents of a tornadic supercell. Cloud Model 1 has also been used to simulate multiple quasi-linear storms and supercells to investigate the mechanisms driving large near-surface vertical vorticity [58].

1.5. Atmospheric Radars and Emulators

Simulated radars can be used alongside atmospheric simulations to analyze their output. Radar is used for detecting and locating reflecting objects [59]. When a radar is activated, electromagnetic energy in the form of microwaves radiated from an antenna propagates in space outward from the radar. The reflecting object (target) intercepts some of the radiated

energy a distance from the radar, and that energy is reflected in many directions. Some of that energy (echo) returns and is received by the radar antenna. The signal is amplified by a receiver and the target is determined to be present if the output exceeds a predetermined threshold. The range of the target is determined through the time the signal takes to travel to the target and back.

The velocity of an object relative to a radar can be determined using the Doppler effect. It describes the change in wave frequency that occurs when there is relative motion between the observer and the wave's source. Specifically, if the observer and source are moving towards each other, the frequency of the wave increases (called a blue shift), and if they are moving apart, the frequency decreases (red shift). This principle enabled the remote measurement of wind speeds, as the movement of air alters the frequency of radar waves reflected from particles in the air.

Radars can be used for many objectives, and there are many targets, including ships, aircraft, missiles, birds, people, meteors, ice, buildings, and precipitation. Radar emulators, such as RSim (the one discussed for this proposal), allow for simulation fields to be scanned similar to the way a physical radar scans an area.

1.5.1. Development of Early Weather Radar

During World War II, the Massachusetts Institute of Technology's Radiation Laboratory realized that the Doppler effect could be employed to measure target velocities through radar systems [60]. At the time, military weather services (such as the Weather Bureau, under the U.S. Army Signal Service) were the only ones able to use radar systems [61]. The Weather Bureau therefore took initiative, and in 1956 developed an experimental, 3-cm, continuous-wave (CW) Doppler weather radar system [60]. While the CW system could not determine the range to a target, there were numerous reports [62] of its success at detecting violent winds near tornadic vortices. In the following years, remote displays from weather radar systems eventually became more widely available for services such as broadcast weather facilities [61].

The 1960s were marked by lighter-weight, solid-state electronics that allowed for the addition of storm avoidance radar in commercial and private aircraft. By 1969, the US Midwest and Southeast had a few television stations with installed radars for weather segments of their news broadcast. With the 1970s came the expansion of more affordable and capable ground-based weather radars [61] and therefore increased systematic documentation by storm-chasers [4]. The first S-band (long wavelength) Doppler weather radar was created by the National Severe Storms Laboratory in Norman, Oklahoma, in 1971 for severe storm studies [63], and dual-Doppler operations began in 1974 after another S-band system [60] was built nearby. The 1980s were marked by the arrival of mobile, ground-based radars able to be mounted on vans, which enabled in situ measurements by storm-chasers [4]. The early 1990s saw the Airborne Doppler radar project tasked with investigating severe convective storms, which led to the VORTEX field experiment from 1994-1995. This decade also saw the teaming up of the Department of Transportation, the Department of Defense, and the Department of Commerce and subsequent fielding of two ground-based Doppler weather radar systems. These systems [61] were named the Next-Generation Weather Radar (now the WSR-88D), and the Terminal Doppler Weather Radar, and have been vital to experiments involving meteorological radar measurements. There now exist many forms technology [4] that aid meteorologists in investigating real-world or simulated weather phenomena: ground-based, mobile, rapid-scan, Doppler radar; mobile, pulsed Doppler lidar; instrumented surface probes; UAVs; mobile, rapid-scan, polarimetric Doppler radar; and radar emulators.

In 2007, an emulator was developed by Ryan May and his colleagues capable of simulating returns from a scanning Doppler radar [64] by using simulated weather features from numerical convective simulations. An emulator is a software or hardware that allows for one system to mimic the output of another system. The simulation of radar data was not a new concept in 2007, as there had previously been emulator-based experiments on time series simulations [65], reflectivity calculations [66], and pulse-based radar return simulations [67]. However, limitations relating to computational requirements prevented these emulators from simulating many aspects of scanning radars, which this 2007 experiment was able to overcome.

1.5.2. RSim Overview

Radar Simulator (RSim) [68] is a dual-polarization (capable of receiving and transmitting pulses in vertical and horizontal polarization orientations) radar emulator developed by the University of Oklahoma Advanced Radar Research Center. RSim utilizes WRF Model data [69] as its input, computing moment data such as spectrum width, radial velocity, and reflectivity factor in the radar domain [68]. This is done by considering the radial velocity and the number concentration of head hydrometer type at every model grid point. The hydrometeor types that RSim accounts for are rain, graupel, snow, and ice.

1.6. Stages of Supercell Tornadogenesis

Advancements in observing, simulating, and emulating tornadoes over the past few decades have significantly improved understanding of the processes behind these phenomena. Until recently, supercell tornadogenesis was described through a three-stage process [70]: formation of a rotating updraft aloft, development of a cyclone at the ground, and the formation of the tornado. Research conducted in recent years has greatly expanded knowledge regarding the third stage, which warranted a new conceptual model [71]. This model splits this third stage into two, resulting in a further refined 4-step conceptual model. As the physical processes associated with tornadogenesis are important for understanding small-scale vorticity, the updated stages are discussed below.

1.6.1. Stage 1: Mesocyclonic Rotation

This first stage is defined by the formation of a mesocyclone. Environmental conditions that support the initiation of this process include warm, moist air being pulled from surrounding areas up into the storm (updraft) and sufficient wind shear. As mentioned previously, wind shear can cause horizontal vorticity. Shown in Figure 3(a), the supercell's updraft of moist air causes the horizontal vorticity to be tilted [31] into the vertical, transforming it into vertical vorticity. For this process [71] to be effective, streamwise vorticity [72] must be present. This occurs when the local rotation axis of the horizontal vorticity is aligned with the storm-relative inflow winds, making the conversion from horizontal to vertical vorticity by the updraft easier. Also essential to this process are the vertical curvature of the updraft, which refers to the bending of the updraft's path as it rises, and shear vorticity [31], the

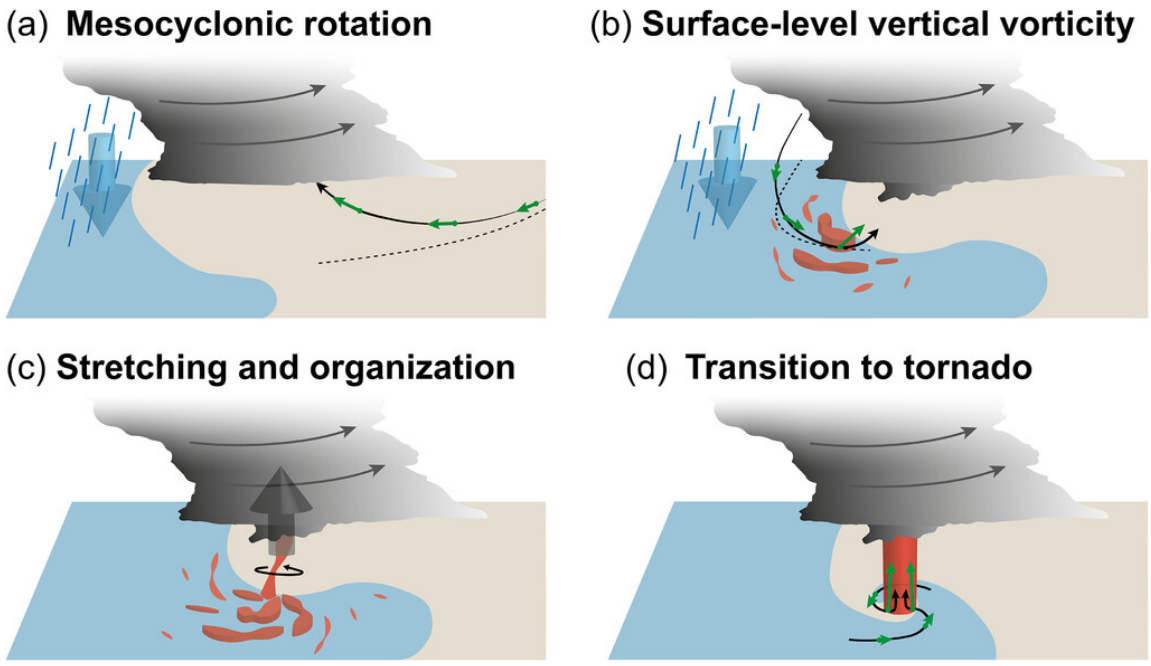

Figure 3. The stages of tornado formation. The images are of the lowest few kilometers of the clouds (shaded gray) as viewed from the rear flank of the supercell. Thin gray arrows indicate the lower portion of the mesocyclone, thin black arrows signify air parcel trajectories, and green vectors show the vorticity's magnitude and direction. Areas shaded in red indicate relatively large vertical vorticity. The thick blue arrows in (a) and (b) indicate the downdraft mentioned in Stage 2 and the thick gray arrow in (c) indicates the vertical pressure gradient acceleration mentioned in Stage 3. Figure taken from Ref. [71].

rotation generated by changes in wind direction and speed with height. The interaction [71] of these processes can feed into the rotation and strengthen the mesocyclone. The mesocyclonic rotation that results creates an area of low pressure in the center, and the upward acceleration of the air due to the updraft creates a region of lower pressure closer to the ground [73]. The upward accelerations driven by these pressure gradients are vital for the stretching of surface-based vertical vorticity later in Stage 3.

Development of this mesocyclonic rotation does not occur throughout the entire supercell in a uniform fashion, as low altitude (about 1 km above the surface) rotation typically intensifies later into what is called a low-level mesocyclone [71]. Stronger low-level mesocyclones are usually associated with stronger lower troposphere vertical wind shear, as the shear creates a more favorable environmental conditions for significant tornadoes [74].

Inflow into low-level mesocyclones has been found to originate very close to the ground (the lowest 500-1000 m [75]), supporting recent model analysis suggesting the potential importance of large horizontal, low-level, streamwise vorticity in tornado production [76]. Strictly tornadic rotation does not arise in this step, as the tilting caused by the updraft is not abrupt enough to cause enough vertical vorticity near the surface [71].

1.6.2. Stage 2: Surface-Level Vertical Vorticity

Consistent surface-level rotation has been shown in many studies to be primarily facilitated by the baroclinic downdraft mechanism [71].

As shown in Figure 3(b), a horizontal buoyancy gradient is generated as air descends in a downdraft and passes through varying temperatures and densities of air layers. The differences in pressure and air density result in the generation of horizontal vorticity. When this vorticity nears the surface, it is tilted vertically, creating a vertically oriented rotating column of air above the surface [77]. This resulting positive (counterclockwise) vertical vorticity near the surface can be strengthened by the alignment of the supercell's updraft and downdraft regions, such that the vorticity from the downdrafts is funneled into the vicinity of the updrafts [78].

These areas of vertical vorticity are typically stretched or structureless in shape, as shown in Figure 4(a). The regions of maximum vorticity are often in proximity [79] and are sometimes called *vortex patches* [71]. The scale of these vortex patches differs between simulations, as does their presence, leading to much uncertainty regarding their behavior and impact on tornado formation. Field observations of them have been sparse, which is believed to be the result of a lack of radars with very high-resolution capability (on the order of a few meters or less). However, improvements are underway, as data [80] from one of the first 3-meter resolution cloud radars were recently analyzed in 2024—a significant advancement compared to the previous cloud radar and lidar systems that had range resolutions of tens of meters. Much uncertainty exists in the vertical and horizontal extent of the vortex patches. These simulated patches tend to be weaker and more amorphous than a typical, mature vortex, and require intensification through stretching and organization to reach that point.

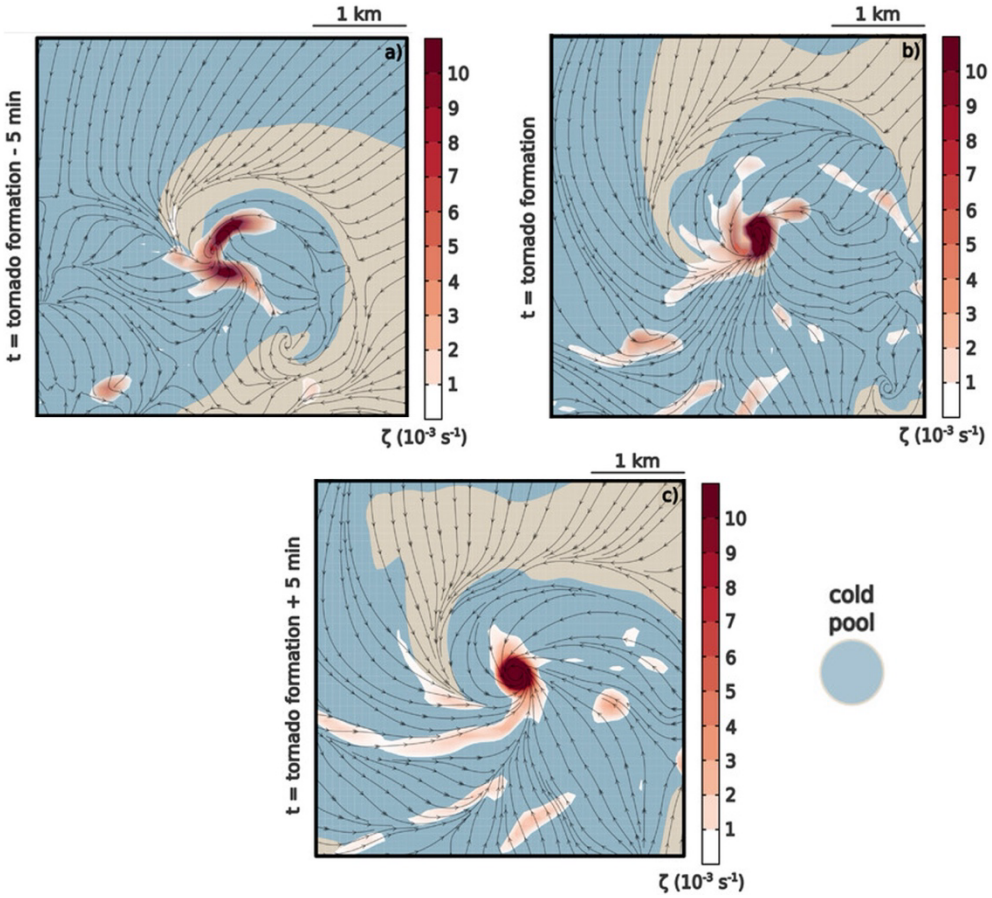

Figure 4. Vortex patches evolving into a mature vortex. The top-down view image was generated by a high-resolution simulation (Δx = 80 m) of a tornadic supercell [75]. The cold pool is shaded in blue and the vertical vorticity at 10 m above ground level is shaded in red (with values scaled by 10^{-3}). The horizontal streamlines at 10 m above ground level (black arrows) were extracted at three times during the storm's formation. The plots show the tornadic region of the supercell (a) 5 min prior to formation, (b) during tornado formation, and (c) 5 min after. Figure adapted from Ref. [71].

1.6.3. Stage 3: Stretching and Organization

The nonuniformly distributed patches of vertical vorticity are noted [71] to organize into a symmetrical vortex over time. This occurs when the patches spiral inward towards a central point and separate areas of rotation merge due to the flow of the supercell or because the vorticity adverts (moves) with the vertical air currents within the storm itself [81], as shown in Figure 3(c) and Figure 4(b). The organized vortex can be formed and maintained in supercells by the convergence of strong winds near the ground [71]. This convergence occurs as air is directed upwards into the low-level mesocyclone by the acceleration of the

air due to a pressure gradient and is potentially sustained by the presence of the rear-flank outflow around the growing rotation. The low-level mesocyclone discussed in Stage 1 is then vital to the stretching and subsequent amplification of the vertical vorticity as the air moves upward.

There are many factors that act against the organization and stretching of the near-surface vertical vorticity, and they are unfortunately difficult to observe [71]. First, the outflow has negative buoyancy, meaning it resists rising and can weaken the vortex [82]. Second, the developing vortex might be pushed away from the optimal region below the mesocyclone due to horizontal airflow [83]. Lastly, sinking air caused by the lowering pressure in the strengthening vortex near the ground can reverse the vertical pressure gradient that aids in the vortex's formation. Regardless, if the constructive factors dominate, a vortex of increasing intensity and symmetry can form and transition into a classic tornado [71].

1.6.4. Stage 4: Transition

The pressure gradient present provides the centripetal force [71] needed to tighten and strengthen the vortex column formed in Stage 3. During this transition stage, surface drag becomes significant in the tornado boundary layer (the lowest few meters above the surface). This drag slows down the rotational speed of the vortex, generating strong inward-pointing horizontal vorticity. At the same time, the slowing of the tangential (sideways) wind reduces the outward force pushing against the vortex, while the centripetal force, driven by the pressure gradient, continues to maintain the inward curvature of the vortex.

Figure 3(d) and Figure 4(c) show the time in which the inwardly accelerated, converging air erupts upward [71], creating a region called the *corner flow*, where the direction of air flow rapidly turns from horizontal to vertical. The combination of violently rising air and surface drag [70] result in damaging vertical and horizontal wind velocities at the ground. It is at this point that tornadogenesis is defined to be complete [71].

1.7. Small-Scale Vorticity

In a recent paper [71] on the updated process of tornadogenesis, it is suggested that the presence and evolution of individual vertical vorticity maxima (vortex patches) prior to the

formation of the mature vortex be investigated. The patches are believed to organize and intensify during Stages 2 and 3, but much is unknown regarding their extent and 3D evolution. To visualize these patches, this proposal suggests coupling a numerical atmospheric model (CM1) with a radar emulator (RSim). Discussing the real-world findings of phenomena related to small-scale patches of vertical vorticity is then vital to determining the input parameters for model and emulator.

1.7.1. Experimental Presence

A study in 2017 by Leigh Orf and his colleagues [84] also mentions these patches. They used CM1 to investigate the El Reno tornadic supercell that spawned a long-lived EF5 tornado on May 24, 2011, in central Oklahoma. The compared supercells (real and simulated) shared characteristics such as long life-span (real: 3 hr, model: 2.5 hr), EF5 intensity of the resulting tornado, duration of tornado (real: 105 min, model: 118 min), and path length (real: 101 km, model: 120 km). It is noted that the modeled supercell did not undergo any cell mergers, while the actual storm was greatly influenced by numerous cell mergers throughout its lifespan [85]. The simulated storm was shown in a preceding study [52] to have taken on physically realistic characteristics as it pertains to hydrometeor fields that were volume-rendered. Specifically, the simulation included characteristics such as a lowering cloud formation beneath the supercell coupled with a stream of warm, moist air being drawn into the storm, smooth cloud structure at lower levels of the simulated atmosphere, and more chaotic, convective cloud structure at higher levels—all of which are routinely observed in real supercell environments.

Once the storm was initialized in the CM1 simulation, it rapidly evolved into a supercell [84]. The storm then split into left- and right-moving cells. Consistent with the typical strengthening of right-moving cells compared to left-movers [86], the right mover began to acquire a hook echo at 500 m above ground level (AGL) and a strong updraft. At t = 3,600 s, the right moving storm had an increasingly pronounced hook in the dBZ reflectivity contour, with the RFD gust front (RFDGF) and the FFD boundary (FFDB) very visible, as shown in Figure 5. A unit used to measure the reflectivity of radar signals in meteorology, dBZ stands for decibels of Z. The “Z” refers to the radar reflectivity factor, which is related to the energy

returned by precipitation particles to the radar. Heavier precipitation reflects more energy back to the radar, and is therefore indicated by higher values of Z. The radar reflectivity factor is usually expressed in decibels, hence the "dB," since the decibel scale is logarithmic—allowing for a wider range of values.

As with other modeled supercells, the region south of the storm's forward flank was characterized by little change in the wind field [87]. The FFDB, located northwest of this area, marked an important boundary in temperature and motion. A strong updraft was evident at this time near the intersection of the FFDB and RFDGF, indicated by the convergence of surface storm-relative wind vectors (Figure 5). As time approached t = 5,000 s, the flow field

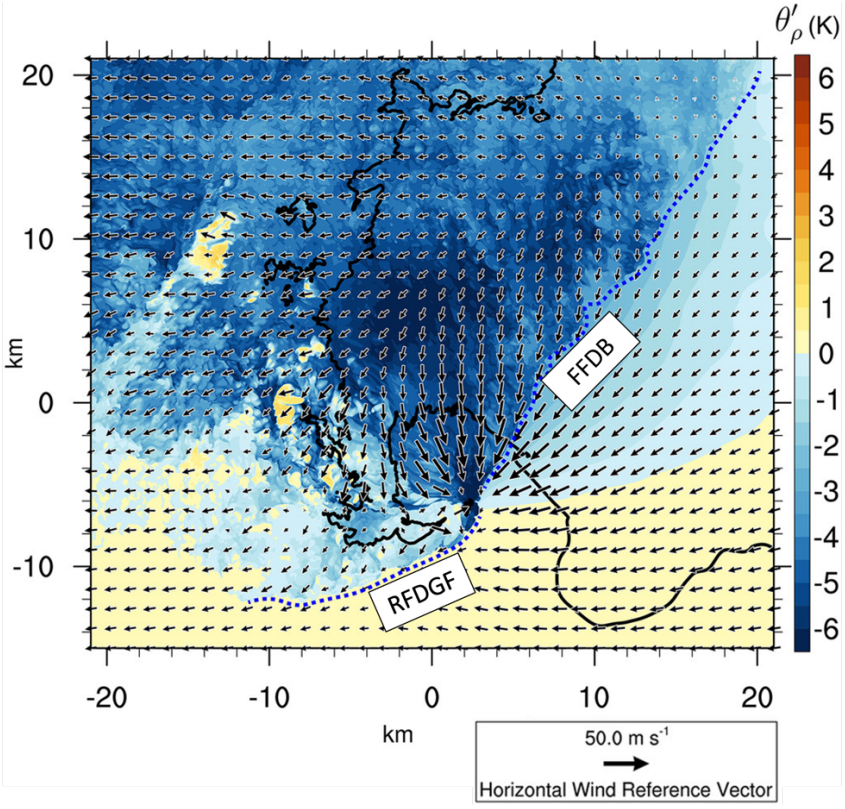

Figure 5. CM1 simulated May 24, 2011, supercell at t = 3,600 s. The thick black line denotes the 500 m AGL 40-dBZ reflectivity contour (moderate rainfall). The colors indicate the perturbation in potential temperature at the surface θ'_ρ in Kelvin. The arrows are storm-relative surface wind vectors plotted every 1.2 km (40th grid point). Figure taken from Ref. [84].

along the FFDB possessed a large amount of vertical vorticity—called a vertical vorticity sheet (VVS). At this time, the paper [84] noted the very complex vertical vorticity structure

along this boundary, as both cyclonic and anticyclonic vorticity patches traversed towards the boundary from within the forward-flank outflow. Moving in a southwestward storm-relative direction similar to the mean velocity vector along the FFDB, the sequence of vortices within the VVS seemed to approach an inflection point (Figure 6). Here, the vortices are noted to have either been swept around and upward by the developing tornado or simply been accumulated by the strengthening vortex.

1.7.2. Importance

Building on the earlier discussion of simulated vertical vorticity [84], the role of pre-tornadic, small-scale vertical vorticity in tornadogenesis remains poorly understood. The importance of understanding the presence, extent, evolution, and effects of this surface vertical vorticity was stressed by Brice Coffer and his colleagues during a 2017 study [79] of 30 supercell simulations from the second Verification of the Origins of Rotation in Tornadoes Experiment (VORTEX2, 88). They investigated tornadic and nontornadic supercells in hopes of finding an environmental trait functioning as a failure point of tornadogenesis—something that

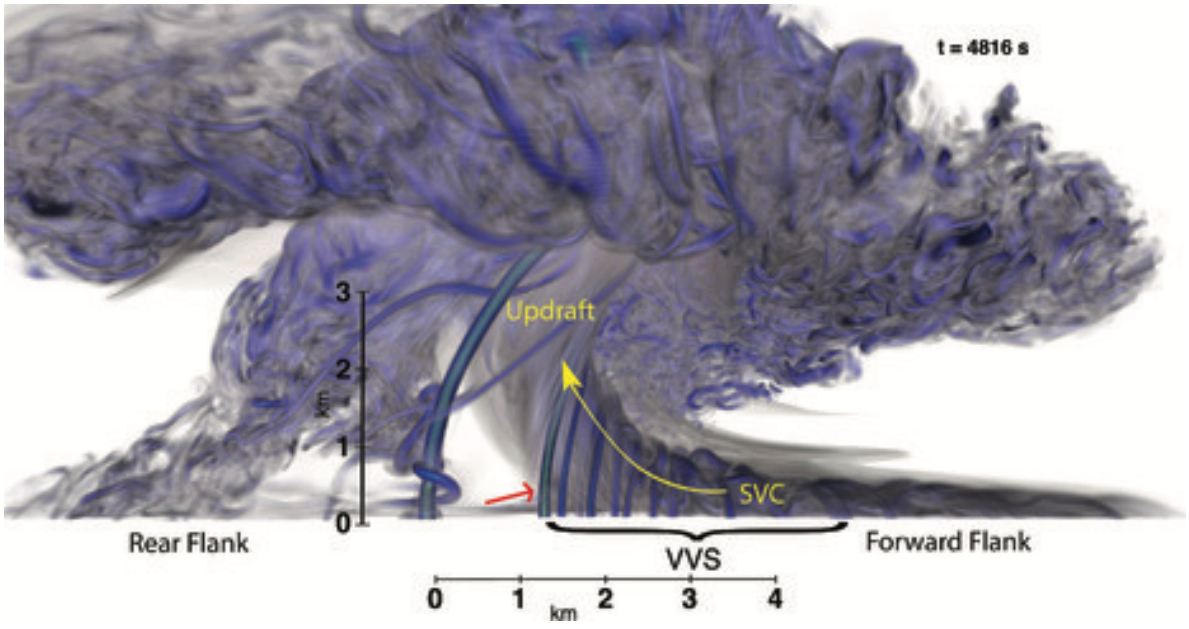

Figure 6. Simulated vorticity magnitude (volume-rendered) at t = 4,816 s. Facing north, the train of vertical vorticity patches within the VVS can be seen moving southwest along the FFDB towards the main vortex (red arrow). The placement of the VVS along the FFDB is shown to influence a current of streamwise vorticity (SVC) feeding into the updraft. Figure taken from Ref [84].

would prohibit the process from continuing. CM1 was used [79] to simulate 15 VORTEX2 nontornadic environments and 15 VORTEX2 tornadic environments. Three of the variables investigated [79] between the tornadic and nontornadic storms are relevant to surface-based vertical vorticity in the tornadogenesis process: reflectivity, maximum updraft, and maximum surface vertical vorticity.

The study [79] outlined a set of criteria that an ensemble member (one of the simulations) had to meet for at least two minutes at any point during the simulation for tornadogenesis to be considered as having occurred. Surface vertical vorticity values needed to exceed 0.3 s^{-1}, the pressure deficit in the vortex needed to exceed 10 hPa over a depth of at least 1 km, and the instantaneous ground-relative wind speeds at 10 m AGL needed to exceed 35 m/s (equivalent to wind speeds of an EF0). The 15 tornadic ensemble members produced a tornadic vortex between t = 51 to 59 min, and the nontornadic members either reached the study's tornadogenesis criteria or failed from t = 62 to 114 min [79]. The reflectivity of each member at the key time of tornadogenesis or failure was plotted in Figure 7 and Figure 8. In a similar fashion, the translated maximum surface vertical vorticity of each member was plotted in Figure 9 and Figure 10. Six of the 15 nontornadic members reached the study's minimum requirements for completed tornadogenesis, with members 7, 10, and 12 (h, k, and m in Figure 7, Figure 8, Figure 9, and Figure 10) being considered very weak, and members 1, 3, and 11 (b, d, and l in Figure 7, Figure 8, Figure 9, and Figure 10) being stronger yet still weaker than any of the tornadic members.

Even though the 15 tornadic ensembles produced much stronger tornadoes than even the "surprise-tornadic" nontornadic ensembles, the reflectivity of each separate model in Figure 7 and Figure 8 is unique—there is no way to confidently identify which is tornadic or nontornadic based solely on reflectivity. Unsurprisingly, reflectivity is not enough to truly gauge how tornadic a supercell is. Looking instead at the translated maximum surface vertical vorticity of each ensemble member (Figure 9 and Figure 10), the tornadic members all exhibited much stronger vorticity—identified by deeper and more condensed values near the tip of the hook echo. The three members of the nontornadic group that produced tornadoes show slightly elevated levels of vertical vorticity near the surface compared to the

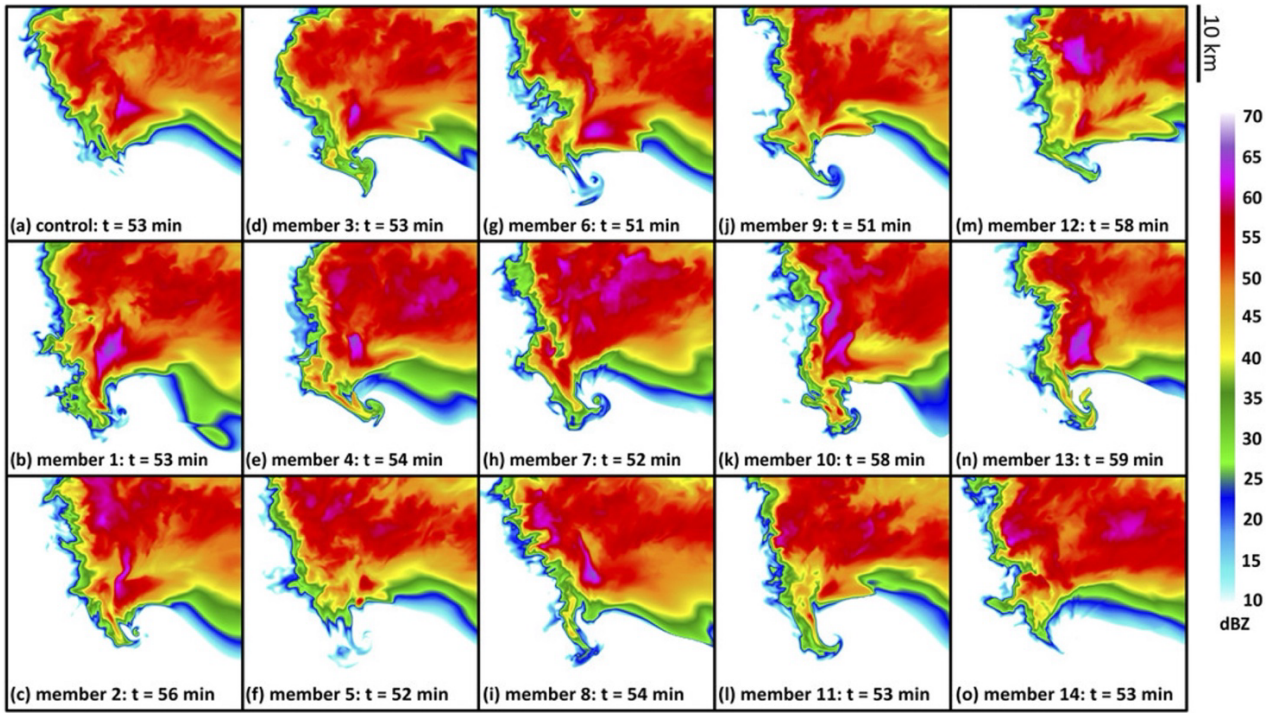

Figure 7. Tornadic VORTEX2 ensembles: reflectivity. Each box contains the horizontal cross section of an ensemble's 10 m AGL reflectivity in dBZ at the key time of tornadogenesis or failure. Figure taken from Ref. [79].

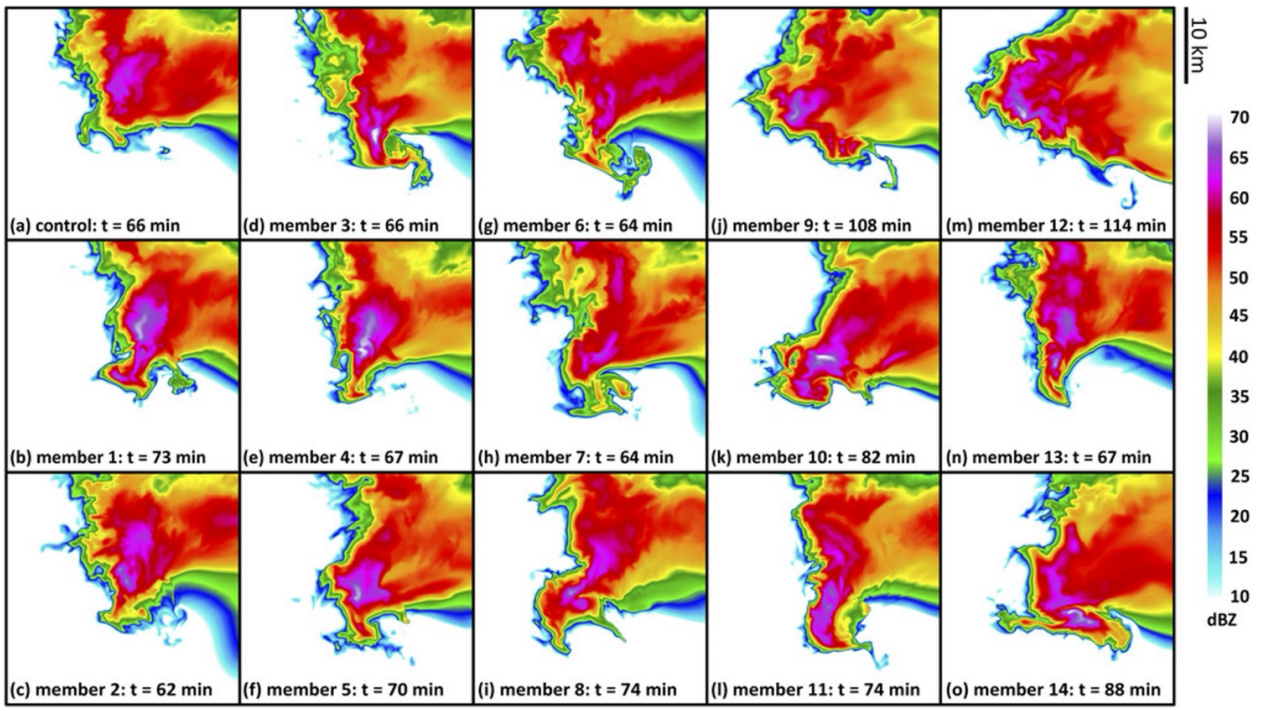

Figure 8. Nontornadic VORTEX2 ensembles: reflectivity. Same as Figure 7, but with nontornadic ensembles. Figure taken from Ref. [79].

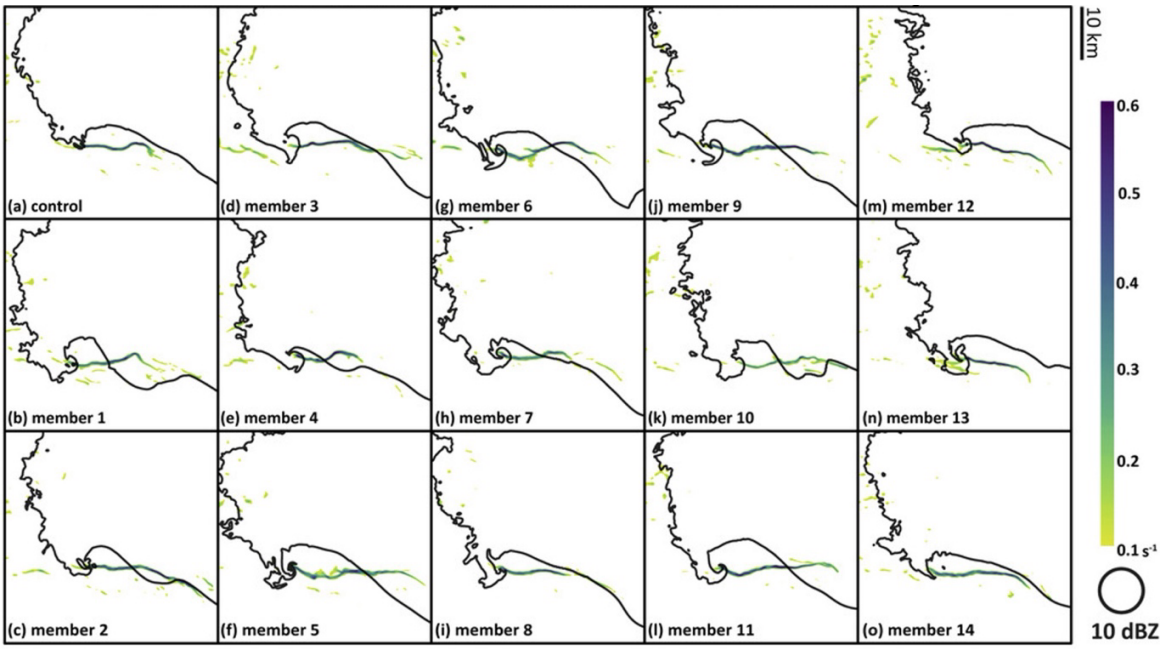

Figure 9. Tornadic VORTEX2 ensembles: translated max surface vertical vorticity. Each box contains horizontal cross sections of the maximum vertical vorticity throughout the simulation's duration. The black line represents the 10 m AGL 10-dBZ reflectivity contour for each key time of tornadogenesis or failure. Figure taken from Ref. [79].

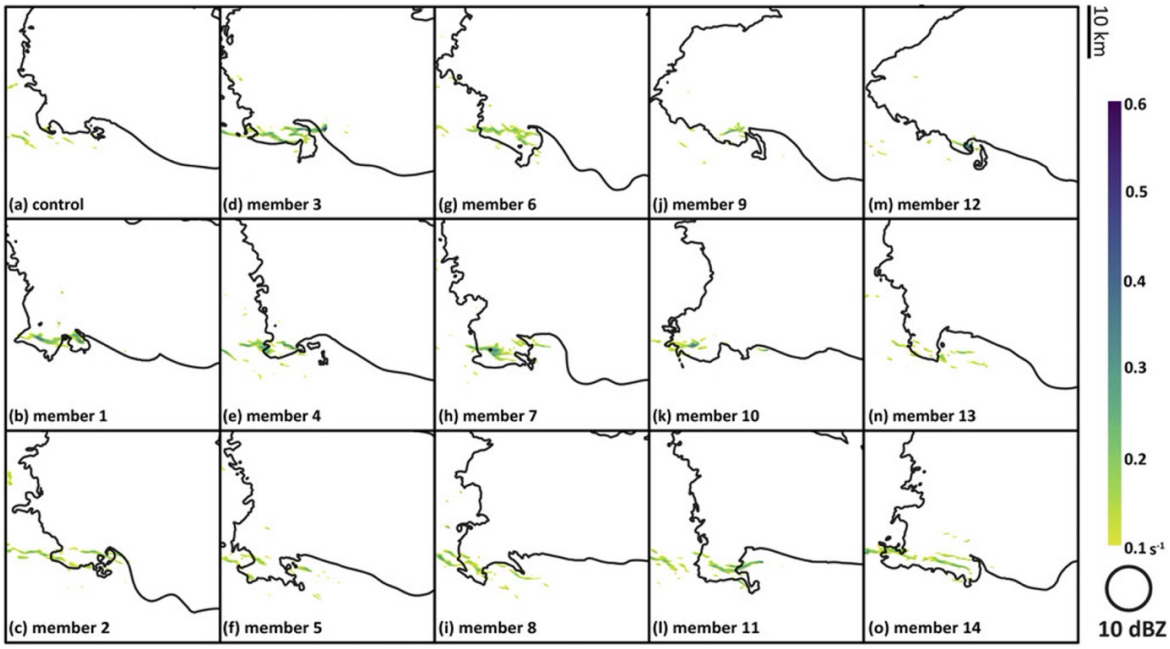

Figure 10. Nontornadic VORTEX2 ensemble: translated max surface vertical vorticity. Same as Figure 9, but with nontornadic ensembles. Figure taken from Ref. [79].

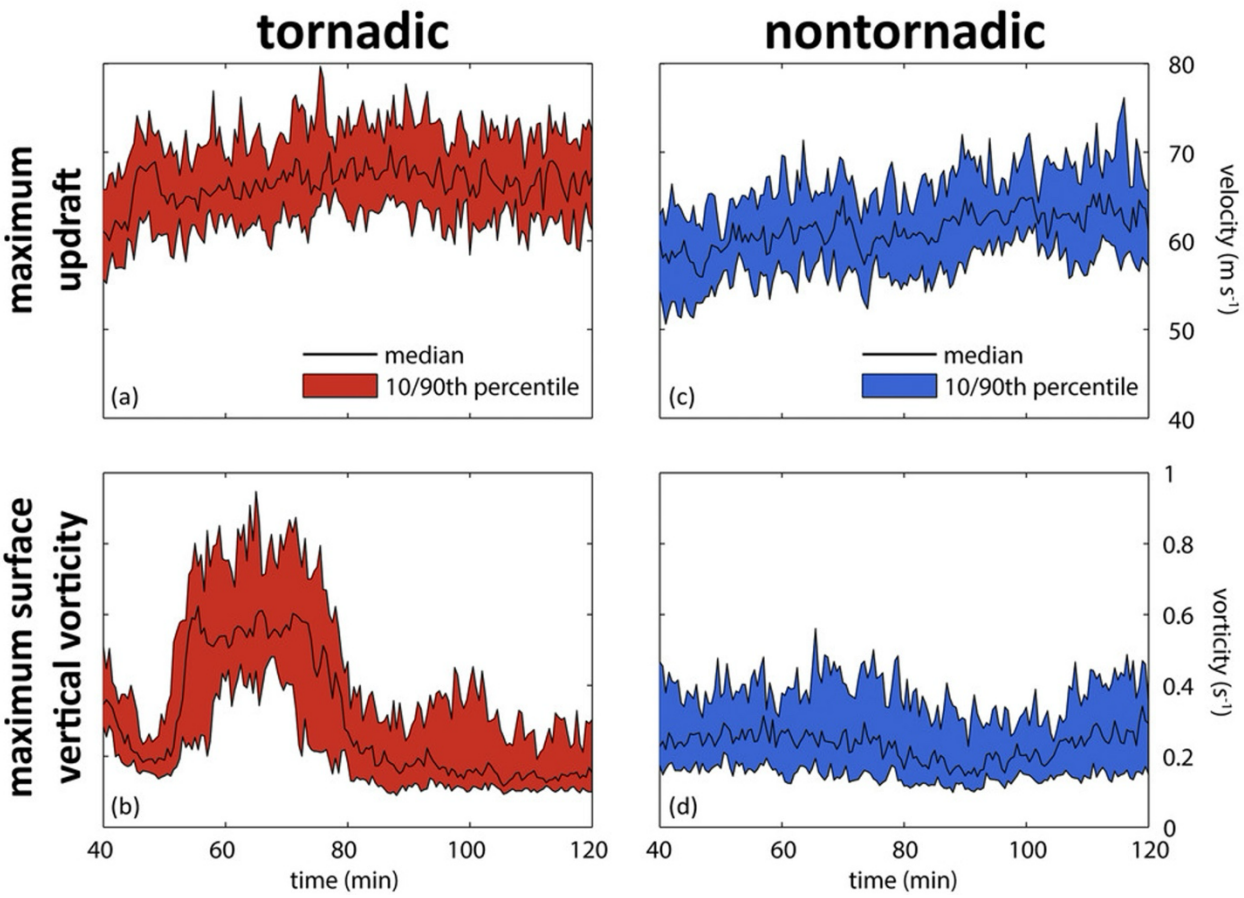

Figure 11. VORTEX2 time comparison of updraft and surface vertical vorticity. The updraft vertical velocity (m/s) for the tornadic (red) and nontornadic (blue) VORTEX2 ensembles is plotted at the top; (a) and (c) respectively. The surface vertical vorticity (s^{-1}) for the tornadic and nontornadic ensembles is plotted at the bottom; (b) and (d) respectively. The black line in each of the time series denotes the median value, and the shaded area represents the 10th to 90th percentiles. Figure taken from Ref. [79].

other nontornadic members as seen in b, d, and l of Figure 10. Another important ingredient for a mature mesocyclone, and therefore tornadogenesis, is a defined updraft [72]. The maximum updraft over time (Figure 11) was compiled for each of the VORTEX2 tornadic and nontornadic members and plotted alongside the maximum surface vertical vorticity of each [79]. Each of the ensemble members were noted to have a strong midlevel updraft (Figure 11a,c), with a mean maximum updraft speed only 5 m/s larger in the tornadic members than the nontornadic members (68 vs 63 m/s). However, with a mean maximum surface vertical vorticity of the tornadic ensemble was nearly twice that of the nontornadic ensemble (0.91 vs 0.47 s^{-1}, Figure 11b,d).

With parameters such as reflectivity and updraft strength failing to categorize tornadic and nontornadic supercells, investigations of near-surface vertical vorticity have become more valuable. The VORTEX2 ensemble simulation experiment [79] highlighted the importance of determining if (and subsequently how) near-surface rotation converges and stretches into a tornadic-strength vortex.

1.8. Motivation

Building on these insights, this proposal addresses findings from the VORTEX2 experiment [79] regarding surface-based vertical vorticity and incorporates a recent simulation [84] that suggests the presence of this vorticity on a previously unobserved, smaller scale. Intrinsic polarimetric variables will be simulated using CM1 [53] and serve as input into the RSim radar. RSim will then emulate Doppler velocity to visualize any pre-tornadic, small-scale vorticity potentially generated by CM1. The radar parameters used by RSim will be adjusted to test different configurations' ability to view on this potential vorticity.

Investigating the numerical simulation's potential generation of small-scale vertical vorticity by using a radar emulator is important to begin an attempt at verifying this phenomenon in the real world. These small-scale vorticity patches have been largely absent in field campaigns, pointing to their potential absence in the real-world or current radar's inability to detect them. This research aims to identify new or updated scanning radar parameters so future field campaigns can attempt to either refute or confirm the presence of these vortex patches.

If the simulated vortex patches are detected with RSim, further investigation will focus on implementing radar sampling strategies that mirror the configuration used in the emulator. This would allow for meteorologists to take a step towards understanding their presence through field observations Another outcome is that the patches are clearly visible in the emulator output when its parameters match those of field observation radars, which did not detect similar phenomena. At this stage, the computational components of the CM1 model will need to be re-evaluated, as it is crucial for simulations to accurately replicate real-world scenarios in the most physically realistic way possible.

Identifying pre-tornadic vorticity and making corresponding changes to field instrumentation would enhance the understanding of tornadogenesis. This improved understanding could, in turn, lead to better forecasting systems and greater accuracy in tornado predictions. Ultimately, this could help reduce the current 75% false-alarm tornado warning rate [2] and the resulting warning fatigue experienced by the public.

Several research collaborators to this proposed research have been identified, including Dr. Jana Houser of the Ohio State University, Dr. Leigh Orf of the University of Wisconsin-Madison, and Dr. David Bodine of the University of Oklahoma. These contributors, coupled with the relevance to the field of meteorology and the potential impact on public safety, make this research an ideal project for a PhD study funded by the National Science Foundation.

Chapter 2

GOVERNING EQUATIONS OF FLUID DYNAMICS

2.1. Overview

Fluid dynamics is the study of the movement of fluids and gases. Atmospheric simulations like CM1 utilize the governing equations of fluid dynamics to calculate atmospheric variables, including temperature and pressure, which can then be visualized in 3D as they evolve over time. These governing equations are built on core principles like the conservation of mass, momentum, and energy. Once those fundamental differential equations are derived, additional factors are incorporated to tailor them for atmospheric conditions, accounting for additional elements such as hydrometeors and processes like phase transitions.

2.2. Fluid Dynamics Derivations

2.2.1. Derivation Setup

There are three governing equations of fluid dynamics [89]: the continuity equation, the momentum equation, and the energy equation. Each is based on a fundamental physics principle; namely, the conservation of mass, of momentum, and of energy, respectively.

An infinitesimal fluid element approach, depicted in Figure 12, will be utilized to derive each of these governing equations.

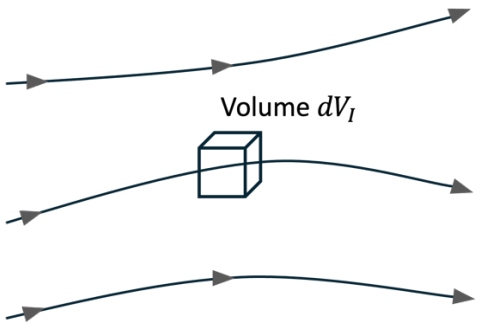

Figure 12. Infinitesimal fluid element approach to fluid dynamics. An infinitesimally small fluid element with differential volume dV_I exists within a flow field. The volume is fixed in space and has fluid flowing through it. Figure adapted from Ref. [89].

In this approach, fluid flow is through an infinitesimal volume dV_I, small enough to be treated as infinitesimal yet large enough to contain many molecules and therefore for the fluid to be considered a continuous medium. The element is fixed in space with fluid moving through it.

The following derivation of the governing equations of fluid dynamics are adapted from Fluid Mechanics 4th Edition [30]. Consider an infinitesimal volume element $dV_I = dx\ dy\ dz$, having sides through which energy, mass and momentum can cross. The fluid velocity field surrounding this element, located at $\vec{r}$ (in Cartesian coordinates (x, y, z)) at time t, is represented by the vector

$$\vec{V}(\vec{r}, t) = \hat{\imath}u(x, y, z, t) + \hat{\jmath}v(x, y, z, t) + \hat{k}w(x, y, z, t)\ , \tag{2}$$

where u, v, and w are the components of the velocity vector. Additionally, all fluid properties are assumed to be continuous functions of position and time. For example, the density is

$$\rho = \rho(x, y, z, t)\ . \tag{3}$$

2.2.2. The Continuity Equation

The continuity equation describes the conservation of mass in the infinitesimal volume. Figure 13 shows the flow of mass through a y-z face of the volume. The dashed boxed filled with dots represents the region of the mass flow ($u\ dt$) that will pass through the y-z face of the volume during time dt. Therefore, the mass entering the volume through that face can be written as

$$(dm)_{yz,in} = \rho u\ dt\ dy\ dz\ , \tag{4}$$

where ρ is constant over dV_I. For a general face, the mass entering the volume is then

$$dm = \rho(x, y, z, t)\left(\vec{V} \cdot \hat{n}\right) dt\ dA\ , \tag{5}$$

where $\hat{n}$ is the unit normal vector to the face of the control volume through which the mass is passing through and dA is the differential area of that surface. This results in a rate of change of the mass inside the volume due to mass crossing the y-z plane

$$\left(\frac{dm}{dt}\right)_{yz,in} = \rho u\ dy\ dz\ . \tag{6}$$

The volume depicted in Figure 14 shows the flow rate of many fluid quantities across the

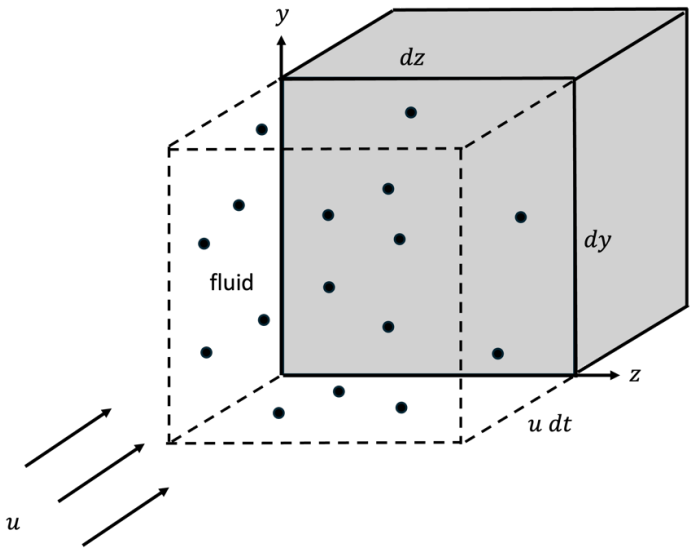

Figure 13. Mass flow into a y-z face of an infinitesimal volume. Fluid with x-direction velocity u flowing through the $dy\ dz$ area element of the volume.

left and righthand $dy\ dz$ faces. The mass flow rate entering the left face of the volume element is defined in Eq. (6) and shown in Figure 14 and the rate mass is leaving the opposite side is given by

$$\left(\frac{dm}{dt}\right)_{yz,out} = \rho(u + du)\ dy\ dz = \left[\rho u + \frac{\partial}{\partial x}(\rho u)\ dx\right]\ dy\ dz \tag{7}$$

since the velocity changes when crossing dx ($du = (du/dx)\ dx$). The change in mass dm/dt inside the volume dV_I with respect to the y-z plane is therefore the rate of flow in minus out:

$$\begin{aligned}\left(\frac{dm}{dt}\right)_{yz} &= \left(\frac{dm}{dt}\right)_{yz,in} - \left(\frac{dm}{dt}\right)_{yz,out} = \rho u\ dy\ dz - \left[\rho u + \frac{\partial}{\partial x}(\rho u)\ dx\right] dy\ dz \\ &= -\frac{\partial}{\partial x}(\rho u)\ dV_I\ .\end{aligned} \tag{8}$$

The flows on the x-y and x-z planes follow a similar pattern, so the rate that the mass changes inside the volume is given by

$$\begin{aligned}\frac{dm}{dt} = \frac{\partial \rho}{\partial t}\ dV_I &= \left(\frac{dm}{dt}\right)_{yz} + \left(\frac{dm}{dt}\right)_{xz} + \left(\frac{dm}{dt}\right)_{xy} \\ &= -\frac{\partial}{\partial x}(\rho u)\ dV_I - \frac{\partial}{\partial y}(\rho v)\ dV_I - \frac{\partial}{\partial z}(\rho w)\ dV_I\ ,\end{aligned} \tag{9}$$

or

$$\frac{\partial \rho}{\partial t} = -\frac{\partial}{\partial x}(\rho u) - \frac{\partial}{\partial y}(\rho v) - \frac{\partial}{\partial z}(\rho w). \tag{10}$$

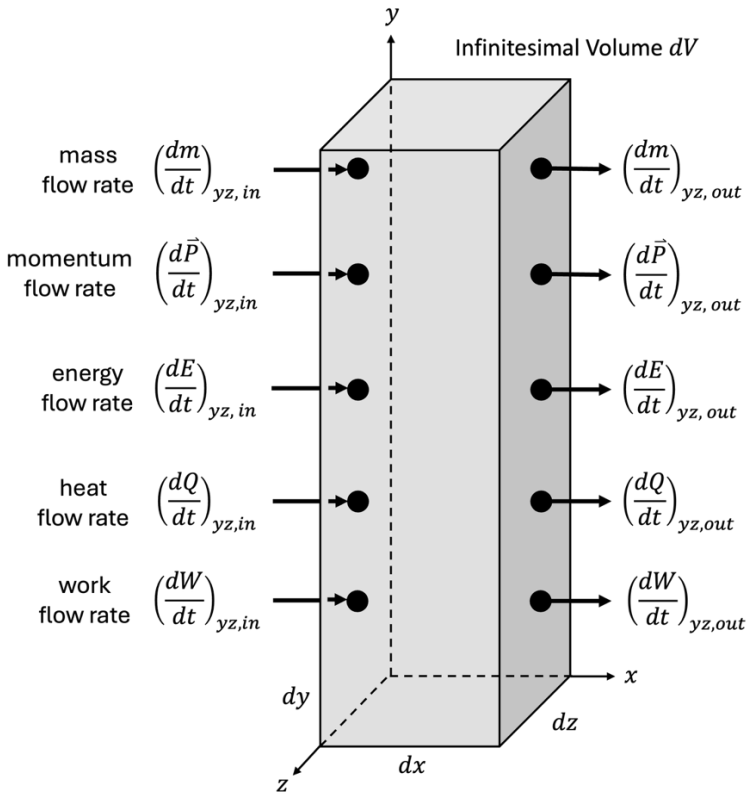

Figure 14. Infinitesimal volume with x-direction fluid properties shown. The volume is labeled with mass, momentum, energy, heat, and work flow rates across the y-z plane.

The only assumption is that the density and velocity are smooth and continuous. The three terms on the right side of Eq. (10) can be rewritten in terms of the divergence, which must be positive if more mass is leaving than entering. This results in the compact form of the continuity equation:

$$\frac{\partial \rho}{\partial t} + \vec{\nabla} \cdot \left(\rho \vec{\mathrm{V}}\right) = 0\,. \tag{11}$$

2.2.3. The Conservation of Momentum Equation

The linear momentum passing through a face of the volume element is

$$d\vec{P} = dm\vec{\mathrm{V}}\,, \tag{12}$$

which means that using Eq. (5) can be used to define the momentum passing into the volume element through the y-z plane

$$\left(d\vec{P}\right)_{yz,in} = \rho u\, dt\, dy\, dz\, \vec{\mathrm{V}}\,. \tag{13}$$

This equation can be generalized, becoming

$$d\vec{P} = \rho(x,y,z,t)\left(\vec{V}\cdot\hat{n}\right) dt\, dA\, \vec{\mathrm{V}}. \tag{14}$$

Therefore, as shown in Figure 14, the rates of change of the momentum entering and leaving the volume through the y-z faces can be written as

$$\left(\frac{d\vec{P}}{dt}\right)_{yz,in} = \rho u\vec{\mathrm{V}}\, dy\, dz \text{ and } \left(\frac{d\vec{P}}{dt}\right)_{yz,out} = \left[\rho u\vec{V} + \frac{\partial}{\partial x}\left(\rho u\vec{V}\right) dx\right] dy\, dz\,. \tag{15}$$

The change in momentum inside the volume element (pertaining to the y-z faces) is then

$$\begin{aligned}\left(\frac{d\vec{P}}{dt}\right)_{yz} &= \left(\frac{d\vec{P}}{dt}\right)_{yz,in} - \left(\frac{d\vec{P}}{dt}\right)_{yz,out} \\ &= \rho u\vec{\mathrm{V}}\, dy\, dz - \left[\rho u\vec{V} + \frac{\partial}{\partial x}\left(\rho u\vec{V}\right) dx\right] dy\, dz \\ &= -\frac{\partial}{\partial x}\left(\rho u\vec{\mathrm{V}}\right) dV_I\,.\end{aligned} \tag{16}$$

Introducing this process in a similar fashion to the x-y and x-z planes as in the previous derivation results in the change in momentum of the infinitesimal volume.

$$\frac{d\vec{P}}{dt} = \frac{\partial}{\partial t}\left(\rho\vec{\mathrm{V}}\right) dV_I = -\left[\frac{\partial}{\partial x}\left(\rho u\vec{\mathrm{V}}\right) + \frac{\partial}{\partial y}\left(\rho v\vec{\mathrm{V}}\right) + \frac{\partial}{\partial z}\left(\rho w\vec{\mathrm{V}}\right)\right] dV_I\,. \tag{17}$$

Therefore, the rate of change of momentum inside the volume element is

$$\frac{d\vec{P}}{dt} = \left[\frac{\partial}{\partial t}\left(\rho\vec{\mathrm{V}}\right) + \frac{\partial}{\partial x}\left(\rho u\vec{\mathrm{V}}\right) + \frac{\partial}{\partial y}\left(\rho v\vec{\mathrm{V}}\right) + \frac{\partial}{\partial z}\left(\rho w\vec{\mathrm{V}}\right)\right] dV_I\,. \tag{18}$$

Applying the product rule on each term, the momentum flow is

$$\begin{aligned}\frac{d\vec{P}}{dt} = \Bigg[&\vec{\mathrm{V}}\frac{\partial\rho}{\partial t} + \rho\frac{\partial\vec{\mathrm{V}}}{\partial t} + \vec{\mathrm{V}}\frac{\partial(\rho u)}{\partial x} + \rho u\frac{\partial\vec{\mathrm{V}}}{\partial x} + \vec{\mathrm{V}}\frac{\partial(\rho v)}{\partial y} + \rho v\frac{\partial\vec{\mathrm{V}}}{\partial y} + \vec{\mathrm{V}}\frac{\partial(\rho w)}{\partial z} \\ &+ \rho w\frac{\partial\vec{\mathrm{V}}}{\partial z}\Bigg] dV_I\,.\end{aligned} \tag{19}$$

Grouping terms with $\vec{\mathrm{V}}$ and ρ results in

$$\frac{d\vec{P}}{dt} = \left(\vec{\mathrm{V}}\left[\frac{\partial \rho}{\partial t} + \frac{\partial(\rho u)}{\partial x} + \frac{\partial(\rho v)}{\partial y} + \frac{\partial(\rho w)}{\partial z}\right] + \rho\left[\frac{\partial \vec{\mathrm{V}}}{\partial t} + u\frac{\partial \vec{\mathrm{V}}}{\partial x} + v\frac{\partial \vec{\mathrm{V}}}{\partial y} + w\frac{\partial \vec{\mathrm{V}}}{\partial z}\right]\right) dV_I \,. \tag{20}$$

The terms within the first set of brackets are identical to those in Eq. (10) which equals the continuity equation (Eq. (11)). Therefore, this grouping equals 0, and the total rate of change of the momentum inside the volume is

$$\frac{d\vec{P}}{dt} = \rho\left[\frac{\partial \vec{\mathrm{V}}}{\partial t} + u\frac{\partial \vec{\mathrm{V}}}{\partial x} + v\frac{\partial \vec{\mathrm{V}}}{\partial y} + w\frac{\partial \vec{\mathrm{V}}}{\partial z}\right] dV_I \,. \tag{21}$$

Based on Eq. (2), the total derivative of the velocity is

$$\frac{d\vec{\mathrm{V}}}{dt} = \frac{\partial \vec{\mathrm{V}}}{\partial t} + u\frac{\partial \vec{\mathrm{V}}}{\partial x} + v\frac{\partial \vec{\mathrm{V}}}{\partial y} + w\frac{\partial \vec{\mathrm{V}}}{\partial z}\,, \tag{22}$$

which shows up Eq. (20). Therefore, the rate of change of the momentum in the volume—also equal to the sum of forces acting on the volume—is

$$\frac{d\vec{P}}{dt} = \sum \vec{F} = \rho\frac{d\vec{\mathrm{V}}}{dt}\, dV_I \,. \tag{23}$$

Pertaining to the left side of this equation, there are two kinds of forces on the volume element: body and surface forces. Body forces act through an external field like gravity, and surface forces are caused by stresses on the sides of the mass. Assuming the fluid is in a uniform gravity field near earth's surface,

$$d\vec{\mathrm{F}}_{grav} = \rho\vec{g}\, dV_I \,, \tag{24}$$

where g is the acceleration of gravity, $\vec{g} = -g\hat{k}$.

Surface forces include the shear (scraping) and normal (compression and tension) stresses acting on the sides of the volume. The force/area on the surface, a "traction" vector $\vec{T}$, can be written as

$$\vec{T} = \vec{\vec{\sigma}} \cdot \hat{n} \,, \tag{25}$$

with $\vec{\vec{\sigma}}$ being the stress tensor and $\hat{n}$ being normal to the surface (with the convention being outward for a closed surface), or

$$T_i = \sum_j \sigma_{ij} n_j \,. \tag{26}$$

So, for example, to find the force/area on the lefthand y-z face,

$$\begin{bmatrix} T_1 \\ T_2 \\ T_3 \end{bmatrix} = \begin{bmatrix} \sigma_{11} & \sigma_{21} & \sigma_{31} \\ \sigma_{12} & \sigma_{22} & \sigma_{32} \\ \sigma_{13} & \sigma_{23} & \sigma_{33} \end{bmatrix} \begin{bmatrix} -1 \\ 0 \\ 0 \end{bmatrix} = -\begin{bmatrix} \sigma_{11} \\ \sigma_{12} \\ \sigma_{13} \end{bmatrix} \text{ or } -\begin{bmatrix} \sigma_{xx} \\ \sigma_{xy} \\ \sigma_{xz} \end{bmatrix} \tag{27}$$

Those stress tensor elements, along with the ones acting on the other faces, are shown in Figure 15. The stresses are the hydrostatic pressure p and viscous stress τ_{ij}, and can be written in matrix form as

$$\sigma_{ij} = \begin{bmatrix} -p + \tau_{xx} & \tau_{yx} & \tau_{zx} \\ \tau_{xy} & -p + \tau_{yy} & \tau_{zy} \\ \tau_{xz} & \tau_{yz} & -p + \tau_{zz} \end{bmatrix}. \tag{28}$$

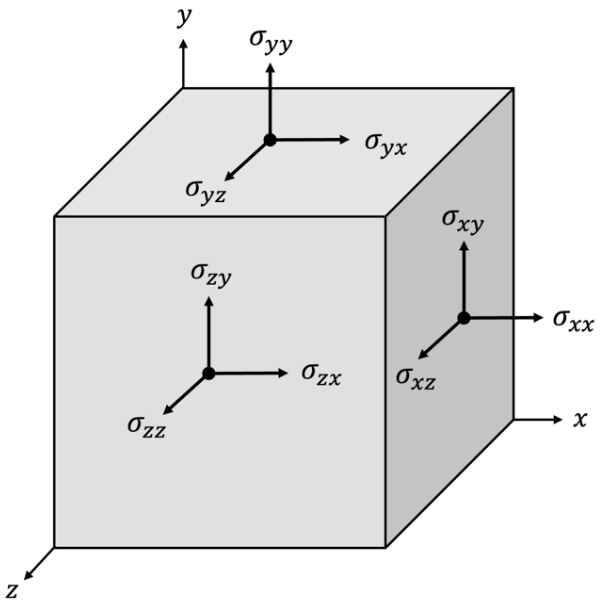

Figure 15. Stress notation. components of the stress tensor are labeled on each face. For example, adding the σ_{xx}, σ_{yx}, and σ_{zx} components results in the sum of the forces in the x direction since there is a force associated with each face. Figure adapted from Ref. [30].

Following a similar methodology as before the momentum flows in terms of stresses can be determined for the y-z faces (Figure 16). Since momentum is a vector, the momentum flow in the x-direction has components on all six faces, which is shown in Figure 15. The x-component of the momentum crossing into the volume through the lefthand y-z face is

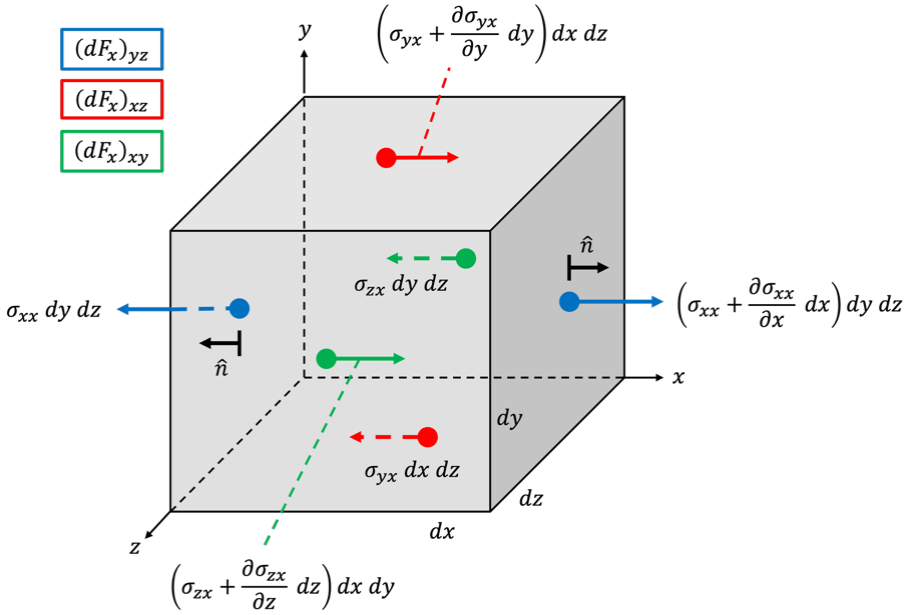

Figure 16. Infinitesimal volume with x direction momentum flow. The momentum in terms of each x-direction stress on the volume element is shown, with blue being the x-direction stress on the y-z faces, red the x-direction stress on the x-z faces, and green the x-direction stress on the x-y faces. Figure adapted from Ref. [30].

$$\left(\frac{dP_x}{dt}\right)_{yz,\,in} = -\sigma_{xx}\, dy\, dz\,, \tag{29}$$

where the normal is in the $-\hat{\imath}$ direction. Similar to the process used to derive Eq. (15), since the stress changes when crossing dx by $(\partial \sigma_{xx}/\,\partial x)\, dx$, the x-component flowing into the righthand y-z face in Figure 16 is positive because the normal is in the $+\hat{\imath}$ direction, and can be written as

$$\left(\frac{dP_x}{dt}\right)_{yz,\,in} = \left(\sigma_{xx} + \frac{\partial \sigma_{xx}}{\partial x}\, dx\right) dy\, dz\,, \tag{30}$$

so that the x-momentum flowing out is therefore

$$\left(\frac{dP_x}{dt}\right)_{yz,\,out} = -\left(\sigma_{xx} + \frac{\partial \sigma_{xx}}{\partial x}\, dx\right) dy\, dz\,. \tag{31}$$

Therefore, the total x-component of the surface force due to the y-z planes is

$$\begin{aligned}(dF_x)_{yz} = \left(\frac{dP_x}{dt}\right)_{yz} &= \left(\frac{dP_x}{dt}\right)_{yz,\,in} - \left(\frac{dP_x}{dt}\right)_{yz,\,out} \\ &= -\sigma_{xx}\, dy\, dz + \left(\sigma_{xx} + \frac{\partial \sigma_{xx}}{\partial x}\, dx\right) dy\, dz = \frac{\partial}{\partial x}(\sigma_{xx})\, dV_I\,.\end{aligned} \tag{32}$$

This can be done for all the planes of the volume element, resulting in

$$\left(\frac{dP_x}{dt}\right) = dF_x = (dF_x)_{yz} + (dF_x)_{xy} + (dF_x)_{xz} = \left[\frac{\partial}{\partial x}(\sigma_{xx}) + \frac{\partial}{\partial y}(\sigma_{yx}) + \frac{\partial}{\partial z}(\sigma_{zx})\right] dV_I. \tag{33}$$

Using the values of the stresses from the matrix in Eq. (28), this net surface force can be expressed as

$$dF_x = \left[-\frac{\partial p}{\partial x} + \frac{\partial}{\partial x}(\tau_{xx}) + \frac{\partial}{\partial y}(\tau_{yx}) + \frac{\partial}{\partial z}(\tau_{zx})\right] dV_I\,. \tag{34}$$

Repeating the previous two steps for y- and z-components results in

$$dF_y = \left[-\frac{\partial p}{\partial y} + \frac{\partial}{\partial x}(\tau_{xy}) + \frac{\partial}{\partial y}(\tau_{yy}) + \frac{\partial}{\partial z}(\tau_{zy})\right] dV_I\,, \tag{35}$$

and

$$dF_z = \left[-\frac{\partial p}{\partial z} + \frac{\partial}{\partial x}(\tau_{xz}) + \frac{\partial}{\partial y}(\tau_{yz}) + \frac{\partial}{\partial z}(\tau_{zz})\right] dV_I\,. \tag{36}$$

Defining the net vector surface force to be

$$d\vec{F}_{surf} = dF_x\hat{\imath} + dF_y\hat{\jmath} + dF_z\hat{k}\,, \tag{37}$$

gives

$$d\vec{F}_{surf} = \left[\left(-\frac{\partial p}{\partial x} + \frac{\partial \tau_{xx}}{\partial x} + \frac{\partial \tau_{yx}}{\partial y} + \frac{\partial \tau_{zx}}{\partial z}\right)\hat{\imath} + \left(-\frac{\partial p}{\partial y} + \frac{\partial \tau_{xy}}{\partial x} + \frac{\partial \tau_{yy}}{\partial y} + \frac{\partial \tau_{zy}}{\partial z}\right)\hat{\jmath} + \left(-\frac{\partial p}{\partial z} + \frac{\partial \tau_{xz}}{\partial x} + \frac{\partial \tau_{yz}}{\partial y} + \frac{\partial \tau_{zz}}{\partial z}\right)\hat{k}\right] dV_I\,. \tag{38}$$

Rearranging, the surface force is

$$d\vec{F}_{surf} = \left[-\vec{\nabla}p + \left(\frac{\partial \tau_{xx}}{\partial x} + \frac{\partial \tau_{yx}}{\partial y} + \frac{\partial \tau_{zx}}{\partial z}\right)\hat{\imath} + \left(\frac{\partial \tau_{xy}}{\partial x} + \frac{\partial \tau_{yy}}{\partial y} + \frac{\partial \tau_{zy}}{\partial z}\right)\hat{\jmath} + \left(\frac{\partial \tau_{xz}}{\partial x} + \frac{\partial \tau_{yz}}{\partial y} + \frac{\partial \tau_{zz}}{\partial z}\right)\hat{k}\right] dV_I\,. \tag{39}$$

The remaining terms in the parentheses can be called the rate of change of viscous stress, with

$$\left(\frac{d\vec{F}}{dV_I}\right)_{viscous} = \left(\frac{\partial \tau_{xx}}{\partial x} + \frac{\partial \tau_{yx}}{\partial y} + \frac{\partial \tau_{zx}}{\partial z}\right)\hat{\imath} + \left(\frac{\partial \tau_{xy}}{\partial x} + \frac{\partial \tau_{yy}}{\partial y} + \frac{\partial \tau_{zy}}{\partial z}\right)\hat{\jmath} + \left(\frac{\partial \tau_{xz}}{\partial x} + \frac{\partial \tau_{yz}}{\partial y} + \frac{\partial \tau_{zz}}{\partial z}\right)\hat{k} = \vec{\nabla}\cdot\overleftrightarrow{\tau}\,, \tag{40}$$

where

$$\overleftrightarrow{\tau} = \begin{bmatrix} \tau_{xx} & \tau_{yx} & \tau_{zx} \\ \tau_{xy} & \tau_{yy} & \tau_{zy} \\ \tau_{xz} & \tau_{yz} & \tau_{zz} \end{bmatrix}. \tag{41}$$

Now, substituting Eq. (40) into Eq. (39), the surface force can be written as

$$d\vec{F}_{surf} = \left[-\vec{\nabla}p + \left(\frac{d\vec{F}}{dV_I} \right)_{viscous} \right] dV_I = \left(-\vec{\nabla}p + \vec{\nabla} \cdot \overleftrightarrow{\tau} \right) dV_I \, . \tag{42}$$

As previously mentioned, the two types of forces considered are body and surface forces. Therefore, the total force on the volume element can be written as

$$d\vec{\mathrm{F}}_{grav} + d\vec{F}_{surf} = \sum \vec{F} \, . \tag{43}$$

Using Eqs. (23), (24), and (42), the conservation of momentum can be expressed as

$$\rho \vec{g} \, dV_I + \left(-\vec{\nabla}p + \vec{\nabla} \cdot \overleftrightarrow{\tau} \right) dV_I = \rho \frac{d\vec{\mathrm{V}}}{dt} \, dV_I \, . \tag{44}$$

Simplifying this expression results in the basic differential momentum equation for an infinitesimal volume element:

$$\rho \vec{g} - \vec{\nabla}p + \vec{\nabla} \cdot \overleftrightarrow{\tau} = \rho \frac{d\vec{\mathrm{V}}}{dt} \, . \tag{45}$$

This expression is often called the Navier-Stokes equation, and it takes into account macroscopic (gravity and pressure) and microscopic (viscosity) forces to balance the forces on a fluid element.

2.2.4. The Conservation of Energy Equation

The differential energy passing through a face of the volume element can be given by

$$dE = h \, dm \, , \tag{46}$$

where the specific enthalpy per unit mass is

$$h = E_s + \frac{p}{\rho} \, , \tag{47}$$

and the specific energy E_s is

$$E_s = U + \frac{1}{2} V^2 + gz \, , \tag{48}$$

where U is the specific internal energy and z is the height above a reference point.

Calling back to a situation akin to Figure 13 and using Eq.(4), the energy crossing an x-face would therefore be

$$(dE)_{yz,in} = h\rho u\, dt\, dy\, dz\,, \tag{49}$$

with the general form of this relationship being

$$dE = h\rho(x,y,z,t)\left(\vec{V}\cdot\hat{n}\right) dt\, dA\,, \tag{50}$$

Like the previous derivations, this energy inside the volume can be defined by the rate of change of the energy entering the volume

$$\left(\frac{dE}{dt}\right)_{yz,in} = hpu\, dy\, dz\,, \tag{51}$$

and leaving

$$\left(\frac{dE}{dt}\right)_{yz,out} = \left[h\rho u + \frac{\partial}{\partial x}(h\rho u)\, dx\right] dy\, dz\,. \tag{52}$$

The change in energy inside the volume element (with respect to the y-z planes) is then

$$\begin{aligned}\left(\frac{dE}{dt}\right)_{yz} = \left(\frac{dE}{dt}\right)_{yz,in} - \left(\frac{dE}{dt}\right)_{yz,out} &= hpu\, dy\, dz - \left[h\rho u + \frac{\partial}{\partial x}(h\rho u)\, dx\right] dy\, dz \\ &= -\frac{\partial}{\partial x}(h\rho u)\, dV_I\end{aligned} \tag{53}$$

Applying this to the energy flowing through the x-z and x-y planes, and including the time derivative of the fluid flow within the volume, the rate of change of the energy inside the volume is

$$\frac{dE}{dt} = \left[\frac{\partial}{\partial t}(\rho E_s) + \frac{\partial}{\partial x}(\rho uh) + \frac{\partial}{\partial y}(\rho vh) + \frac{\partial}{\partial z}(\rho wh)\right] dV_I. \tag{54}$$

This rate of change of energy can be expressed through heat and work by

$$\frac{dE}{dt} = \frac{dQ}{dt} - \frac{dW}{dt} = \left[\frac{\partial}{\partial t}(\rho E_s) + \frac{\partial}{\partial x}(\rho uh) + \frac{\partial}{\partial y}(\rho vh) + \frac{\partial}{\partial z}(\rho wh)\right] dV_I\,, \tag{55}$$

where dQ/dt is the rate of heat entering the system and dW/dt is the rate of work done by the fluid's pressure as it moves through the volume. To simplify this expression, a process like the derivation of the conservation of momentum is used, where terms are grouped such that the continuity equation appears. The last three terms of the equation can be combined using the definition of the velocity vector field, since

$$\frac{\partial}{\partial x}(\rho u h) + \frac{\partial}{\partial y}(\rho v h) + \frac{\partial}{\partial z}(\rho w h) = \rho h\left(\frac{\partial u}{\partial x} + \frac{\partial v}{\partial y} + \frac{\partial w}{\partial z}\right) = \vec{\nabla} \cdot \rho \vec{\mathrm{V}} h \,. \tag{56}$$

Using the definition of h from Eq. (47) and introducing Eq. (56) into Eq. (55) results in

$$\frac{dQ}{dt} - \frac{dW}{dt} = \left[\frac{\partial}{\partial t}(\rho E_s) + \vec{\nabla} \cdot \rho \vec{\mathrm{V}}\left(E_s + \frac{p}{\rho}\right)\right] dV_I \,, \tag{57}$$

Using the product rule for divergence, this becomes

$$\frac{dQ}{dt} - \frac{dW}{dt} = \left[\frac{\partial}{\partial t}(\rho E_s) + \vec{\nabla} \cdot \rho \vec{\mathrm{V}} E_s + \vec{\nabla} \cdot p \vec{\mathrm{V}}\right] dV_I \,, \tag{58}$$

and using the product rules for differential and divergence, this then becomes

$$\frac{dQ}{dt} - \frac{dW}{dt} = \left[E_s \frac{\partial \rho}{\partial t} + \rho \frac{\partial E_s}{\partial t} + E_s\left(\vec{\nabla} \cdot \rho \vec{\mathrm{V}}\right) + \rho \vec{\mathrm{V}} \cdot \vec{\nabla} E_s + p\left(\vec{\nabla} \cdot \vec{\mathrm{V}}\right) + \vec{\mathrm{V}} \cdot \vec{\nabla} p\right] dV_I \,. \tag{59}$$

Grouping terms leads to

$$\frac{dQ}{dt} - \frac{dW}{dt} = \left[E_s\left(\frac{\partial \rho}{\partial t} + \vec{\nabla} \cdot \rho \vec{\mathrm{V}}\right) + \rho\left(\frac{\partial E_s}{\partial t} + \vec{\mathrm{V}} \cdot \vec{\nabla} E_s\right) + p\left(\vec{\nabla} \cdot \vec{\mathrm{V}}\right) + \vec{\mathrm{V}} \cdot \vec{\nabla} p\right] dV_I \,, \tag{60}$$

in which the continuity equation appears inside the parentheses of the first term. The continuity term therefore disappears as well as the third term if the fluid is incompressible ($\vec{\nabla} \cdot \vec{\mathrm{V}} = 0$). With an incompressible fluid, the divergence of the velocity vector field is zero since there are no net sinks or sources of fluid within the flow. In this case,

$$\frac{dQ}{dt} - \frac{dW}{dt} = \left[\rho\left(\frac{\partial E_s}{\partial t} + \vec{\mathrm{V}} \cdot \vec{\nabla} E_s\right) + \vec{\mathrm{V}} \cdot \vec{\nabla} p\right] dV_I \,. \tag{61}$$

The total time derivative of the specific energy is

$$\frac{dE_s}{dt} = \frac{\partial E_s}{\partial x}\frac{\partial x}{\partial t} + \frac{\partial E_s}{\partial y}\frac{\partial y}{\partial t} + \frac{\partial E_s}{\partial z}\frac{\partial z}{\partial t} + \frac{\partial E_s}{\partial t}, \tag{62}$$

resulting in

$$\frac{dE_s}{dt} = \frac{\partial E_s}{\partial t} + \vec{\mathrm{V}} \cdot \vec{\nabla} E_s \,. \tag{63}$$

Introducing this relationship into the density term of Eq. (61) and moving the differential volume to the other side yields an updated relation of energy flow into the volume element of

$$\frac{dQ}{dt} - \frac{dW}{dt} = \left(\rho \frac{dE_s}{dt} + \vec{\mathrm{V}} \cdot \vec{\nabla} p\right) dV_I \,. \tag{64}$$

Neglecting radiation and only considering heat flow by conduction, dQ/dt can be evaluated using Fourier's law of heat conduction

$$\vec{\mathrm{q}} = -k\vec{\nabla}T\,, \tag{65}$$

where k is the thermal conductivity, which relates $\vec{\mathrm{q}}$ (the vector rate of heat flow per unit area) to the gradient of the temperature $\vec{\nabla}T$. For the y-z plane, heat flow rate into the volume element (as shown in Figure 14) is

$$\left(\frac{dQ}{dt}\right)_{yz,in} = -k\frac{\partial T}{\partial x}\,dy\,dz\,, \tag{66}$$

and the flow out is

$$\left(\frac{dQ}{dt}\right)_{yz,out} = -\left[k\frac{\partial T}{\partial x} + \frac{\partial}{\partial x}\left(k\frac{\partial T}{\partial x}\right)\,dx\right]\,dy\,dz\,. \tag{67}$$

The change in heat flow inside the volume element with respect to the y-z planes is then

$$\begin{aligned}\left(\frac{dQ}{dt}\right)_{yz} &= \left(\frac{dQ}{dt}\right)_{yz,in} - \left(\frac{dQ}{dt}\right)_{yz,out} \\ &= -k\frac{\partial T}{\partial x}\,dy\,dz\, - \left(-\left[k\frac{\partial T}{\partial x} + \frac{\partial}{\partial x}\left(k\frac{\partial T}{\partial x}\right)\,dx\right]\,dy\,dz\right) \\ &= \frac{\partial}{\partial x}\left(k\frac{\partial T}{\partial x}\right)dV_I = k\frac{\partial^2 T}{\partial x^2}dV_I\,.\end{aligned} \tag{68}$$

Conducting this with the x-z and x-y faces, the rate of change of the energy inside the volume due to heat flow is

$$\frac{dQ}{dt} = k\frac{\partial^2 T}{\partial x^2}dV_I + k\frac{\partial^2 T}{\partial y^2}dV_I + k\frac{\partial^2 T}{\partial z^2}\,dV_I = -\vec{\nabla}\cdot\vec{\mathrm{q}}\,dV_I\,. \tag{69}$$

This shows that heat flow is proportional to the element volume. Using Fourier's law in Eq. (65) and noting that Eq. (69) is defined by heat leaving the volume element,

$$\frac{dQ}{dt} = \vec{\nabla}\cdot\left(k\vec{\nabla}T\right)\,dV_I. \tag{70}$$

Power can be expressed as

$$\mathcal{P} = \frac{dW}{dt} = \vec{F}\cdot\vec{V}\,. \tag{71}$$

In this case, the force per unit area is the traction force (Eq. (25)), so the rate of change of energy crossing a plane due to work flow is

$$\frac{dW}{dt} = (\overleftrightarrow{\sigma}\cdot\hat{n})\cdot\vec{V}\,dA. \tag{72}$$

Using Eq. (26), this can be expressed in index notation where dA is the surface and n is normal to the surface,

$$\left(\frac{dW}{dt}\right)_{n,A} = \sum_i \left(\sum_j \sigma_{ji} n_j \right) v_i \, dA \, . \tag{73}$$

For example, the normal to the $dA = dy\, dz$ surface at $x = 0$ (as in Figure 14) is $-\hat{\imath}$. Writing this in matrix form,

$$\begin{aligned} \left(\frac{dW}{dt}\right)_{in,yz} &= \begin{bmatrix} v_x & v_y & v_z \end{bmatrix} \begin{bmatrix} \sigma_{xx} & \sigma_{yx} & \sigma_{zx} \\ \sigma_{xy} & \sigma_{yy} & \sigma_{zy} \\ \sigma_{xz} & \sigma_{yz} & \sigma_{zz} \end{bmatrix} \begin{bmatrix} -1 \\ 0 \\ 0 \end{bmatrix} dy\, dz \\ &= -\begin{bmatrix} v_x & v_y & v_z \end{bmatrix} \begin{bmatrix} \sigma_{xx} \\ \sigma_{xy} \\ \sigma_{xz} \end{bmatrix} dy\, dz \\ &= -\left(v_x \sigma_{xx} + v_y \sigma_{xy} + v_z \sigma_{xz} \right) dy\, dz \, . \end{aligned} \tag{74}$$

The hydrostatic pressure terms are absent from this expression, as the pressure is already accounted for in Eq. (64). If the flow of energy is due to only viscous stress and not pressure, then the energy flow into the volume through the y-z plane (as shown in Figure 14) is

$$\left(\frac{dW}{dt}\right)_{yz,in} = -\left(u\tau_{xx} + v\tau_{xy} + w\tau_{xz} \right) dy\, dz \, . \tag{75}$$

The energy flow out is then

$$\left(\frac{dW}{dt}\right)_{yz,out} = \left[\left(u\tau_{xx} + v\tau_{xy} + w\tau_{xz} \right) + \frac{\partial}{\partial x} \left(u\tau_{xx} + v\tau_{xy} + w\tau_{xz} \right) dx \right] dy\, dz \, . \tag{76}$$

and the total energy flow leaving the volume element through the y-z faces is

$$\begin{aligned} \left(\frac{dW}{dt}\right)_{yz} &= \left(\frac{dW}{dt}\right)_{yz,in} - \left(\frac{dW}{dt}\right)_{yz,out} \\ &= -\left(u\tau_{xx} + v\tau_{xy} + w\tau_{xz} \right) dy\, dz \\ &\quad - \left[\left(u\tau_{xx} + v\tau_{xy} + w\tau_{xz} \right) + \frac{\partial}{\partial x} \left(u\tau_{xx} + v\tau_{xy} + w\tau_{xz} \right) dx \right] dy\, dz \\ &= -\Bigg[2\left(u\tau_{xx} + v\tau_{xy} + w\tau_{xz} \right) \\ &\quad + \frac{\partial}{\partial x} \left(u\tau_{xx} + v\tau_{xy} + w\tau_{xz} \right) dx \Bigg] dy\, dz. \end{aligned} \tag{77}$$

Adding the energy flow through each surface of the volume element, this work flow rate becomes

$$\frac{dW}{dt} = -\Big[2\big(u\tau_{xx} + v\tau_{xy} + w\tau_{xz}\big) + \frac{\partial}{\partial x}\big(u\tau_{xx} + v\tau_{xy} + w\tau_{xz}\big) + 2\big(u\tau_{yx} + v\tau_{yy} + w\tau_{yz}\big) + \frac{\partial}{\partial y}\big(u\tau_{yx} + v\tau_{yy} + w\tau_{yz}\big) + 2\big(u\tau_{zx} + v\tau_{zy} + w\tau_{zz}\big) + \frac{\partial}{\partial z}\big(u\tau_{zx} + v\tau_{zy} + w\tau_{zz}\big)\Big]\, dV_I \tag{78}$$

which, for an infinitesimally small volume element, can be simplified to

$$\frac{dW}{dt} = -\vec{\nabla}\cdot\big(\vec{\mathrm{V}}\cdot\vec{\tau}\big)\, dV_I. \tag{79}$$

Substituting the net viscous-work rate and Eq. (70) into Eq. (64),

$$\rho\frac{dE_s}{dt} + \vec{\mathrm{V}}\cdot\vec{\nabla}p = \vec{\nabla}\cdot\big(k\vec{\nabla}T\big) + \vec{\nabla}\cdot\big(\vec{\mathrm{V}}\cdot\vec{\tau}\big)\,. \tag{80}$$

By splitting up the viscous-work term, the expression

$$\vec{\nabla}\cdot\big(\vec{\mathrm{V}}\cdot\vec{\tau}\big) = \vec{\mathrm{V}}\cdot\big(\vec{\nabla}\cdot\vec{\tau}\big) + \Phi \tag{81}$$

arises, where Φ is the viscous-dissipation function

$$\Phi = \mu\left[2\left(\frac{\partial u}{\partial x}\right)^2 + 2\left(\frac{\partial v}{\partial y}\right)^2 + \left(\frac{\partial w}{\partial w}\right)^2 + \left(\frac{\partial v}{\partial x} + \frac{\partial u}{\partial y}\right)^2 + \left(\frac{\partial w}{\partial y} + \frac{\partial v}{\partial z}\right)^2 + \left(\frac{\partial u}{\partial z} + \frac{\partial w}{\partial x}\right)^2\right]. \tag{82}$$

Since the terms are all quadratic, Φ is always positive, meaning that a viscous flow always loses available energy to dissipative work—following the second law of thermodynamics. By substituting Eq. (81) into Eq. (80), the new expression becomes

$$\rho\frac{dE_s}{dt} + \vec{\mathrm{V}}\cdot\vec{\nabla}p = \vec{\nabla}\cdot\big(k\vec{\nabla}T\big) + \vec{\mathrm{V}}\cdot\big(\vec{\nabla}\cdot\vec{\tau}\big) + \Phi\,. \tag{83}$$

Then, using the conservation of linear momentum equation (Eq. (45)) to eliminate $\vec{\nabla}\cdot\vec{\tau}$ results in

$$\rho\frac{dE_s}{dt} + \vec{\mathrm{V}}\cdot\vec{\nabla}p = \vec{\nabla}\cdot\big(k\vec{\nabla}T\big) + \vec{\mathrm{V}}\cdot\left(\rho\frac{d\vec{\mathrm{V}}}{dt} - \rho\vec{g} + \vec{\nabla}p\right) + \Phi\,. \tag{84}$$

Canceling $\vec{\mathrm{V}}\cdot\vec{\nabla}\,p$ from both sides, and using Eq. (48), Eq. (84) becomes

$$\rho\left[\frac{dU}{dt} + \frac{1}{2}\frac{d}{dt}V^2 + \frac{d}{dt}(gz)\right] = \vec{\nabla}\cdot\big(k\vec{\nabla}T\big) + \vec{\mathrm{V}}\cdot\left(\rho\frac{d\vec{\mathrm{V}}}{dt} - \rho\vec{g}\right) + \Phi\,. \tag{85}$$

By rewriting the $(d/dt)V^2$ term as

$$\frac{d}{dt}V^2 = \frac{d}{dt}\left(\vec{\mathrm{V}}\cdot\vec{\mathrm{V}}\right) = \vec{\mathrm{V}}\cdot\frac{d\vec{\mathrm{V}}}{dt} + \frac{d\vec{\mathrm{V}}}{dt}\cdot\vec{\mathrm{V}} = 2\vec{\mathrm{V}}\cdot\frac{d\vec{\mathrm{V}}}{dt}, \tag{86}$$

and assuming $\vec{g} = -g\vec{k}$,

$$\vec{\mathrm{V}}\cdot(-\rho\vec{g}) = \rho\frac{dz}{dt}g = \rho\frac{d}{dt}(gz), \tag{87}$$

Eq. (85) can be expressed as

$$\rho\left[\frac{dU}{dt} + \frac{1}{2}\frac{d}{dt}V^2 + \frac{d}{dt}(gz)\right] = \vec{\nabla}\cdot\left(k\vec{\nabla}T\right) + \frac{1}{2}\rho\frac{d}{dt}V^2 + \rho\frac{d}{dt}(gz) + \Phi. \tag{88}$$

Canceling out like terms results in

$$\rho\frac{dU}{dt} = \vec{\nabla}\cdot\left(k\vec{\nabla}T\right) + \Phi, \tag{89}$$

which is the most typical form of the general differential conservation of energy equation for an incompressible fluid.

2.3. Connections to the Cloud Model 1

The continuity, momentum, and energy equations, Eqs. (11), (45), and (89), respectively, govern fluid dynamics, and form the basis of the CM1 simulation. The governing equations of CM1 [91, 92] include additional terms that describe a moist atmosphere that are nonhydrostatic and compressible as opposed to the hydrostatic, incompressible equations discussed earlier.

CM1's governing equations for velocity [90] are

$$\frac{\partial u}{\partial t} + c_p\theta_p\frac{\partial\pi'}{\partial x} = ADV(u) + fv + D_u + N_u, \tag{90}$$

$$\frac{\partial v}{\partial t} + c_p\theta_p\frac{\partial\pi'}{\partial y} = ADV(v) - fu + D_v + N_v, \text{and} \tag{91}$$

$$\frac{\partial w}{\partial t} + c_p\theta_p\frac{\partial\pi'}{\partial z} = ADV(w) + B + D_w + N_w. \tag{92}$$

These equations are written in terms of the non-dimensional pressure, π, and density potential temperature θ_p. They describe the same physics as Eq. (45), which can be written as

$$\rho\frac{d\vec{\mathrm{V}}}{dt} + \vec{\nabla}p = \rho\vec{g} + \vec{\nabla}\cdot\vec{\tau}. \tag{93}$$

Using Eq. (22), this becomes

$$\frac{\partial \vec{\mathrm{V}}}{\partial t} + \frac{1}{\rho}\vec{\nabla}p = -u\frac{\partial \vec{\mathrm{V}}}{\partial x} - v\frac{\partial \vec{\mathrm{V}}}{\partial y} - w\frac{\partial \vec{\mathrm{V}}}{\partial z} + \vec{g} + \frac{\vec{\nabla}\cdot\vec{\tau}}{\rho}. \tag{94}$$

Splitting this expression up for each of the axes, as CM1's governing equations for velocity [90] are written, results in

$$\frac{\partial u}{\partial t} + \frac{1}{\rho}\frac{\partial p}{\partial x} = ADV(u) + 0 + \left(\frac{\vec{\nabla}\cdot\vec{\tau}}{\rho}\right)_x, \tag{95}$$

$$\frac{\partial v}{\partial t} + \frac{1}{\rho}\frac{\partial p}{\partial y} = ADV(v) + 0 + \left(\frac{\vec{\nabla}\cdot\vec{\tau}}{\rho}\right)_y, \text{and} \tag{96}$$

$$\frac{\partial w}{\partial t} + \frac{1}{\rho}\frac{\partial p}{\partial z} = ADV(w) + g + \left(\frac{\vec{\nabla}\cdot\vec{\tau}}{\rho}\right)_z, \tag{97}$$

with

$$ADV(u) = -u\frac{\partial u}{\partial x} - v\frac{\partial u}{\partial y} - w\frac{\partial u}{\partial z}, \tag{98}$$

$$ADV(v) = -u\frac{\partial v}{\partial x} - v\frac{\partial v}{\partial y} - w\frac{\partial v}{\partial z}, \text{and} \tag{99}$$

$$ADV(w) = -u\frac{\partial w}{\partial x} - v\frac{\partial w}{\partial y} - w\frac{\partial w}{\partial z}. \tag{100}$$

The right side of the CM1 velocity and derived equations contain an advection (transport) operator term ADV dependent on the component of the velocity. The stress term in each of the derived equations is accounted for in various regimes of CM1's velocity equations to account for friction with the surface and viscosity. They appear as diffusion terms (D) that represent the diffusive tendencies in the system and Newtonian relaxation terms (N) that model the dampening of the fluid. Also included in Eqs. (95), (96), and (97) are terms pertaining to the Coriolis force (the force due to Earth's rotation) and a buoyancy term (B).

Although the velocity equations in CM1 may not immediately appear to bear a strong resemblance to the fundamental conservation of momentum equation in fluid dynamics, they are, in fact, more complex and specialized formulations derived from it.

Chapter 3

PROPOSED CM1 AND RSIM METHODOLOGY AND ANALYSIS

3.1. Overview

As a relatively young field of science, much is unknown in the realm of severe weather. Modern technology has allowed meteorologists to begin to understand more regarding tornadogenesis, but there is still much to learn pertaining to the finer details of this process. A recent study [84] using a numerical simulation [53] built from the principles of fluid dynamics [30] reported small-scale, pre-tornadic vertical vorticity as being present in their simulation. This proposed study aims to explore the potential existence of pre-tornadic, small-scale vertical vorticity through numerical simulations and radar emulation, with the goal of advancing understanding of the tornadogenesis process. CM1 will take atmospheric variables measured in the May 24, 2011, El Reno environment [84] as input and calculate polarimetric variables for multiple hydrometeor types. These variables will serve as input into RSim, which will emulate radar retrievals of reflectivity and Doppler velocity. The parameters of the radar emulator, such as wavelength and range resolution, will be changed until simulated pre-tornadic, small-scale vorticity is visualized, or all configurations are exhausted.

3.2. Proposal

A flow diagram of the proposed methodology is displayed in Figure 17, which begins with the CM1 numerical simulation. The CM1 code [53] will be initialized using the El Reno environment [84] from May 24, 2011, which generated a violent tornado and simulated small-scale vortex patches. These simulations will be run on a supercomputer. Each NetCDF (Network Common Data Form) file generated by the CM1 model will represent the physical state of the atmosphere over time at intervals of a few seconds within the model domain (the specific region of the atmosphere simulated by the model), including wind, moisture, temperature, and pressure. NetCDF files are a standardized format used for storing multi-dimensional data and are commonly used in scientific computing with large datasets.

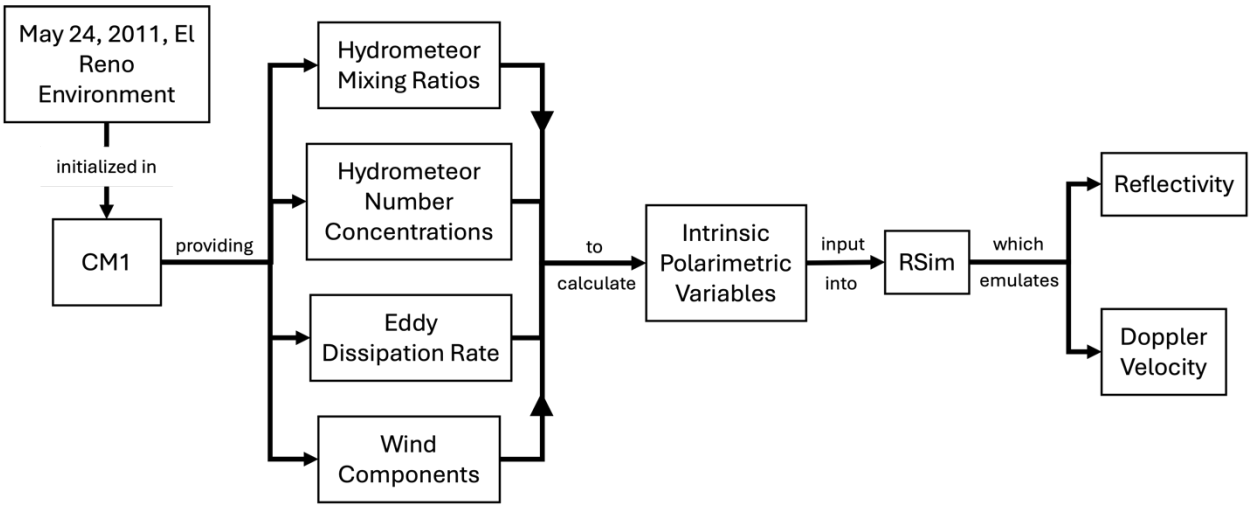

Figure 17. Flow diagram of methodology. The proposed experiment involves initializing the May 24, 2011, El Reno atmospheric environment in CM1. The resulting atmospheric simulation will provide hydrometeor mixing ratios, hydrometeor number concentrations, the eddy dissipation rate, and wind components, all of which will be used to calculate intrinsic polarimetric variables over time. These variables will serve as input into RSim, which will emulate reflectivity and Doppler velocity.

Hydrometeor mixing ratios, hydrometeor number concentrations, wind components, and the eddy dissipation rate from the simulation will be used to calculate polarimetric variables for multiple hydrometeor types over time and space. These variables, which describe the polarization state of electromagnetic waves and are essential for modeling radar-atmosphere interactions, will be stored in NetCDF files by CM1 and serve as input for the RSim emulator. The hydrometeor mixing ratio refers to the mass of water (in any form) present in the air relative to the mass of dry air, and the eddy dissipation rate describes the rate at which turbulent energy is converted into heat due to chaotic motion and friction within a fluid. These intrinsic polarimetric variables, such as differential reflectivity (which provides insight into the shape and orientation of hydrometeors) and the co-polar coefficient (which indicates the similarity in shape and size of the scanned hydrometeors) serve as key inputs into RSim. These variables are fundamental to radar backscatter, as they help characterize the physical properties and dynamics of the simulated atmosphere.

RSim will then simulate radar reflectivity retrievals, which measure how intense the precipitation is, using the values of the liquid water mixing ratio (the amount of liquid water per unit mass of dry air). It will use an approximated drop size distribution based on the mass-weighted drop diameter, which represents the average size of raindrops within a CM1 grid volume, with larger drops having more influence on the average due to their greater mass. Additionally, RSim will emulate Doppler velocity—the variable that could show the vortex patches—by calculating the radial velocity component of the motion from the model-based wind field, the derived reflectivity values, and the location of the hypothetical radar that is scanning the storm.

RSim parameters will be systematically changed each time the emulator is run to test if simulated pre-tornadic, small-scale vorticity can be detected in the emulator output with different configurations. Parameters that can be changed include the radar wavelength, range resolution, azimuthal (horizontal) resolution, pulse repetition time, mechanical rotation rate, beamwidth, range from the storm, and volume coverage pattern. The values of each parameter of each configuration will be pre-determined based on data from past and current field radars, as well as configurations that could realistically be developed with existing technologies. As a preliminary baseline, a typical X-band (0.03 m wavelength) mobile radar, such as the RaXPol radar [91], commonly used in field campaigns, will be emulated. Some of the parameters of RaXPol [91] include a beamwidth of 1.0°, a transmit pulse width of 0.1-40 μs, a pedestal scan rate of 180° s^{-1} in azimuth, and a range resolution of 30 m. Since numerous field campaigns (TORUS [92] and VORTEX2 [88]) have not reported seeing the vortex patches in question using their X-band radars, it is expected that this baseline emulator setting will not detect them.

To allow for precise repeatability, any areas of small-scale rotation will be identified by a program created to locate areas of weak to moderate outbound velocities (moving away from the radar) adjacent to weak to moderate inbound velocities (moving toward the radar) within RSim's outputted radar display. The focus will be on the intensity of the velocities and the size of the rotating regions. The temporal and spatial evolution of the vorticity patches will be tracked by the autonomous monitoring the positions of the individual vorticity

maxima, allowing for an investigation of how these patches behave as a tornado forms nearby. Previous simulations, including [77] and [93], which explored vertical vorticity in relation to tornadogenesis, as well as the simulation [84] that identified some small-scale vertical vorticity as regions of localized vorticity maxima, indicate that most vertical vorticity occurs on scales ranging from a few hundred meters to several kilometers. Given that this proposal focuses on small-scale vorticity, the primary emphasis is on rotation occurring at scales ranging from 10 meters to a few hundred meters.

The RSim configuration will be changed, as described previously, until all devised emulator configurations are exhausted. If the emulator's results indicate the parameters typical of traditional mobile radars should be sufficient to resolve the small-scale near-surface vortex patches, a systematic effort will be undertaken to locate these patches in historic datasets. If the emulator's results indicate that small-scale near-surface vortex patches should be resolved by a radar with a configuration not used in field research, this configuration will be explored in more depth through RSim and then potentially be suggested for construction in an upcoming field project. Another possibility is that no configuration of radar parameters reveals the vortex patches. In this case, the parameters that identified the small-scale vorticity from the May 24, 2011, El Reno environment [84] will be explored, as these patches were identified by that simulation.

Chapter 4

OVERVIEW AND NEXT STEPS

4.1. Overview

Tornadogenesis, a newly emerging area of study within the broader field of atmospheric science, explores the formation and evolution of tornadoes. This field originated, as did many others, under the umbrella of atmospheric science, with the kickstarting of United States meteorological observation collections [7] around 1870. With the first successful tornado forecast [16] in 1948, which followed over 50 years of a forecast ban [11, 12, 13, 14, 15] on tornadoes due to concerns of public panic, research [17, 19] in this field blossomed in the middle of the 20th century. Tornadogenesis theories came into existence in 1979 [29], with the conceptual models still being updated today [32, 70, 71].

A main focus of these theories is on the generation and evolution of near-surface vertical vorticity, on which many studies [33, 34, 35] have been conducted in the last few decades. Since physical observations of smaller-scale phenomena such as tornadoes and tornadic vertical vorticity are difficult to obtain, convective numerical simulations have been developed to depict and study the behaviors of generated storms [39]. CM1 [53], which numerically solves the conservation of mass, momentum, and energy governing equations [90] of fluid dynamics [30], is one of the more recent atmospheric simulations, and is frequently used to investigate [55, 56, 57, 58] simulated supercells. Radar emulators such as RSim [68] can be used alongside atmospheric simulations to analyze their output and mirror radars used in field operations.

Mentioned in a study [84] that used CM1 to investigate a tornadic supercell near the town of El Reno, Oklahoma, on May 24, 2011, as well as a paper [71] on an updated conceptual process of tornadogenesis, the spatiotemporal evolution of small-scale vertical vorticity prior to the formation of a tornadic vortex is relatively unknown. Simulation-based evidence [84] suggests that this vertical vorticity may occur on a smaller scale than observed in field

experiments. Verifying these results is crucial for understanding tornadogenesis, as near-surface vertical vorticity has been linked [79] to tornado-producing supercells.

Using a supercomputer, the May 24, 2011, El Reno environment [84] will be initialized in CM1. Polarimetric variables for multiple hydrometeor types will be calculated and serve as input into RSim, which will emulate radar retrievals of reflectivity and Doppler velocity. The configurations of the radar emulator (such as wavelength and range resolution) will be changed in an attempt to visualize the simulated pre-tornadic small-scale vertical vorticity mentioned in the study [84] which initialized this environment. If the returns from the emulator indicate that a radar configuration like those used in recent field experiments can visualize this vorticity, an attempt will be made to locate these phenomena in historic datasets. If the results indicate that a configuration unlike any that currently exist can resolve the vorticity, further research will be conducted on this configuration and upgrade recommendations for current field radars may be written.

4.2. Next Steps

The research described in this thesis is intended to form the basis of a PhD research proposal under the direction of Dr. Jana Houser from the Ohio State University, Dr. Leigh Orf from the University of Wisconsin-Madison, and Dr. David Bodine from the University of Oklahoma. Dr. Houser's expertise using mobile radar observations to study tornadogenesis and access to radar data (such as RaXPol, DOW, and Ka-Band) will provide a strong foundation for the radar-emulation and analysis portions of the project. Dr. Orf will provide the CM1 simulation of the May 24, 2011, El Reno storm [84], and support the analysis thereof. Dr. Bodine will provide the code and support for the RSim radar emulator. This project is expected to take two years, with no weather-dependent delays or time-sensitive field observations expected as it relies primarily on previously collected data. A publication in the American Meteorological Society's (AMS) Weather and Forecasting peer-reviewed journal detailing the research is anticipated, as well as a publication in the Journal of Atmospheric and Oceanic Technology covering the radar/emulator comparisons or proposing new mobile radars for vorticity data collection. The results of this study could also be presented at the AMS's Fall 2026 Severe Local Storms conference and the winter 2027 AMS annual meeting.

References

[1] M. J. Woods, R. J. Trapp, H. M. Mallinson, Geophys. Res. Lett. **50**, e2023GL104796 (2023).
[2] J. A. Brotzge, S. Erickson, H. Brooks, Weather and Forecasting **26**, 534 (2011).
[3] J. A. Brotzge, S. E. Nelson, R. L. Thompson, B. T. Smith, Weather and Forecasting **28**, 1261 (2013).
[4] H. B. Bluestein, *Severe Convective Storms and Tornadoes: Observations and Dynamics* (Springer, 2013), Chap. 6.
[5] T. T. Fujita, Satellite and Mesometeorology Research Project **91** (1971).
[6] T. Marshall, T. Brown-Giammanco, S. N. Krautwurst, N. L. De Toledo, in 30th Conference on Severe Local Storms, Santa Fe, NM, 2022 (unpublished).
[7] M. Bradford, Weather and Forecasting **14**, 484 (1999).
[8] J. P. Finley, United States of America War Department Professional Papers of the Signal Service No. 7: Report on the Character of Six Hundred Tornadoes (1884).
[9] J. P. Finley, Journal of the Franklin Institute **121**, 241 (1886).
[10] J. P. Finley, Science **3**, 766 (1884).
[11] A. W. Greenley, Annual Report of the Chief Signal Officer of the Army to the Secretary of War for the Year 1887: Part 1, 1887 (unpublished).
[12] H. A. Hazen, *The Tornado* (N. D. C. Hodges, New York, 1890), p. 124.
[13] C. F. Marvin, Weather Bureau Library No. 36313 (1915).
[14] W. L. Gregg, Weather Bureau Library No. 77883 (1934).
[15] W. L. Moore, Weather Bureau Library No. 25594 (1905).
[16] R. C. Miller and C. A. Crisp, Weather and Forecasting **14**, 479 (1999).
[17] S. F. Corfidi, Weather and Forecasting **14**, 507 (1999).
[18] R. G. Beebe, Bulletin of the American Meteorological Society **38**, 575 (1957).
[19] J. O. Galway, Weather and Forecasting **7**, 564 (1992).
[20] K. A. Browning, Journal of the Atmospheric Sciences **21**, 634 (1964).
[21] E. L. Van Tassel, Monthly Weather Review **83**, 255 (1955).
[22] G. E. Stout and F. A. Huff, Bulletin of the American Meteorological Society **34**, 281 (1953).
[23] P. M. Markowski, Monthly Weather Review **130**, 852 (2002).
[24] R. Rotunno and H. B. Bluestein, Rep. Prog. Phys. **87**, 114801 (2024).
[25] P. S. Ray, R. J. Doviak, G. B. Walker, D. Sirmans, J. Carter, B. Bumgarner, Journal of Applied Meteorology and Climatology **14**, 1521 (1975).
[26] J. B. Klemp, R. B. Wilhelmson, P. S. Ray, Journal of the Atmospheric Sciences **38**, 1558 (1981).
[27] J. B. Klemp, Annual Review of Fluid Mechanics **19**, 369 (1987).
[28] G. S. Forbes, Monthly Weather Review **109**, 1457 (1981).
[29] L. R. Lemon and C. A. Doswell III, Monthly Weather Review **107**, 1184 (1979).
[30] F. M. White, *Fluid Mechanics*, edited by J. P. Holman and J. Lloyd (McGraw-Hill College, 1998), 4th ed.
[31] J. M. L. Dahl, Journal of the Atmospheric Sciences **74**, 2997 (2017).

[32] P. M. Markowski and Y. P. Richardson, Journal of the Atmospheric Sciences **71**, 243 (2014).
[33] R. Davies-Jones and H. Brooks, Mesocylogenesis from a Theoretical Perspective in *The Tornado: Its Structure, Dynamics, Prediction, and Hazards*, edited by C. Church, D. Burgess, C. Doswell, R. Davies-Jones (1993), Geophysical Monograph Series Vol. 79.
[34] R. J. Trapp and M. L. Weisman, Monthly Weather Review **131**, 2804 (2003).
[35] R. Rotunno, P. M. Markowski, G. H. Bryan, Journal of the Atmospheric Sciences **74**, 1757 (2017).
[36] B. Roberts, M. Xue, A. D. Schenkman, D. T. Dawson II, Journal of the Atmospheric Sciences **73**, 3371 (2016).
[37] B. Roberts and M. Xue, Journal of the Atmospheric Sciences **74**, 3055 (2017).
[38] B. Roberts, M. Xue, D. T. Dawson II, Journal of the Atmospheric Sciences **77**, 1699 (2020).
[39] R. B. Wilhelmson and L. J. Wicker, Numerical Modeling of Severe Local Storms in *Severe Convective Storms*, edited by C. A. Doswell (American Meteorological Society, Boston, MA, 2001).
[40] Y. Ogura, A Review of Numerical Modeling Research on Small Scale Convection in the Atmosphere in *Severe Local Storms* (American Meteorological Society, Boston, MA, 1963), Meteorological Monographs Vol. 5.
[41] T. L. Clark, J. Comput. Phys. **24**, 186 (1977).
[42] R. A. Anthes and T. T. Warner, Monthly Weather Review **106**, 1045 (1978).
[43] J. Dudhia, Monthly Weather Review **121**, 1493 (1993).
[44] D. Zhang and R. A. Anthes, Journal of Applied Meteorology and Climatology **21**, 1594 (1982).
[45] S. G. Benjamin and T. N. Carlson, Monthly Weather Review **114**, 307 (1986).
[46] E. Hsie, R. A. Anthes, D. Keyser, Journal of the Atmospheric Sciences **41**, 2581 (1984).
[47] D. Zhang and J. M. Fritsch, Journal of the Atmospheric Sciences **43**, 1913 (1986).
[48] G. J. Tripoli, Monthly Weather Review **120**, 1342 (1992).
[49] L. J. Wicker and W. C. Skamarock, Monthly Weather Review **126**, 1992 (1998).
[50] L. J. Wicker and R. B. Wilhelmson, Journal of the Atmospheric Sciences **52**, 2675 (1995).
[51] G. H. Bryan and J. M. Fritsch, Monthly Weather Review **130**, 2917 (2002).
[52] L. Orf, R. B. Wilhelmson, L. J. Wicker, Parallel Computing **55**, 28 (2016).
[53] D. G. Bryan, *CM1 Homepage*, https://www2.mmm.ucar.edu/people/bryan/cm1/ (Accessed 23 January 2025), 2025.
[54] M. Vich and R. Romero, Atmospheric Research **290**, 106784 (2023).
[55] V. Spiridonov, M. Ćurić, G. Velinov, B. Jakimovski, Atmospheric Research **261**, 105758 (2021).
[56] A. R. Wade and M. D. Parker, Journal of the Atmospheric Sciences **78**, 1389 (2021).
[57] A. Schueth, C. Weiss, J. M. L. Dahl, Monthly Weather Review **149**, 1651 (2021).
[58] C. H. Boyer and J. M. L. Dahl, Monthly Weather Review **148**, 4281 (2020).
[59] M. I. Skolnik, *Introduction to Radar Systems* (McGraw0Hill Book Company, 1981), 2nd ed., Chap. 1.

[60] R. C. Whiton, P. L. Smith, S. G. Bigler, K. E. Wilk, A. C. Harbuck, Weather and Forecasting **13**, 244 (1998).
[61] R. C. Whiton, P. L. Smith, S. G. Bigler, K. E. Wilk, A. C. Harbuck, Weather and Forecasting **13**, 219 (1998).
[62] R. L. Smith and D. W. Holmes, Monthly Weather Review **89**, 1 (1961).
[63] D. Sirmans and R. J. Doviak, Journal of Applied Meteorology and Climatology **12**, 694 (1973).
[64] R. M. May, M. I. Biggerstaff, M. Xue, Journal of Atmospheric and Oceanic Technology **24**, 1973 (2007).
[65] D. S. Zrnić, Journal of Applied Meteorology and Climatology **14**, 619 (1975).
[66] V. Chandrasekar and V. N. Bringi, Journal of Atmospheric and Oceanic Technology **4**, 464 (1987).
[67] C. Capsoni and M. D'Amico, Journal of Atmospheric and Oceanic Technology **15**, 593 (1998).
[68] A. Mahre, T. Yu, D. J. Bodine, Journal of Atmospheric and Oceanic Technology **37**, 1955 (2020).
[69] W. C. Skamarock, J. B. Klemp, J. Dudhia, D. O. Gill, D. M. Barker, M. G. Duda, X. Huang, W. Wang, J. G. Powers, NCAR Technical Note: A Description of the Advanced Research WRF Version 3, 2008.
[70] R. Davies-Jones, Atmospheric Research **158**, 274 (2015).
[71] J. Fischer, J. M. L. Dahl, B. E. Coffer, J. L. Houser, P. M. Markowski, M. D. Parker, C. C. Weiss, A. Schueth, Bulletin of the American Meteorological Society **105**, E1084 (2024).
[72] R. Davies-Jones, Journal of the Atmospheric Sciences **41**, 2991 (1984).
[73] N. A. Goldacker and M. D. Parker, Journal of the Atmospheric Sciences **78**, 2763 (2021).
[74] R. L. Thompson, B. T. Smith, J. S. Grams, A. R. Dean, C. Broyles, Weather and Forecasting **27**, 1136 (2012).
[75] B. E. Coffer, M. D. Parker, J. M. Peters, A. R. Wade, Monthly Weather Review **151**, 2205 (2023).
[76] B. E. Coffer, M. Taszarek, M. D. Parker, Weather and Forecasting **35**, 2621 (2020).
[77] M. D. Parker and J. M. L. Dahl, Monthly Weather Review **143**, 2795 (2015).
[78] C. C. Weiss, D. C. Dowell, J. L. Schroeder, P. S. Skinner, A. E. Reinhart, P. M. Markowski, Y. P. Richardson, Monthly Weather Review **143**, 2736 (2015).
[79] B. E. Coffer, M. D. Parker, J. M. L. Dahl, L. J. Wicker, A. J. Clark, Monthly Weather Review **145**, 4605 (2017).
[80] Z. Zhu, F. Yang, P. Kollias, K. Lamer, E. Luke, J. B. Mead, Y. M. Sua, A. M. Vogelmann, A. McComiskey, Bulletin of the American Meteorological Society **105**, E2010 (2024).
[81] J. M. L. Dahl, Monthly Weather Review **148**, 3533 (2020).
[82] P. M. Markowski, J. M Straka, E. N. Rasmussen, Monthly Weather Review **130**, 1692 (2002).
[83] J. Fischer and J. M. L. Dahl, Monthly Weather Review **151**, 23 (2022).
[84] L. Orf, R. Wilhelmson, B. Lee, C. Finley, A. Houston, Bulletin of the American Meteorological Society **98**, 45 (2017).

[85] R. L. Tanamachi, P. L. Heinselman, L. J. Wicker, Weather and Forecasting **30**, 501 (2015).
[86] J. B. Klemp and R. B. Wilhelmson, Journal of the Atmospheric Sciences **35**, 1097 (1978).
[87] J. Beck and C. Weiss, Monthly Weather Review **141**, 649 (2013).
[88] J. Wurman, D. Dowell, Y. Richardson, P. Markowski, E. Rasmussen, D. Burgess, L. Wicker, H. B. Bluestein, Bulletin of the American Meteorological Society **93**, 1147 (2012).
[89] J. D. Anderson Jr., *Computational Fluid Dynamics*, edited by J. F. Wendt (Springer Berlin, Heidelberg, 1992), 1st ed., Chap. 2.
[90] G. H. Bryan, The Governing Equations for CM1, 2013 (unpublished).
[91] A. L. Pazmany, J. B. Mead, H. B. Bluestein, J. C. Snyder, J. B. Houser, Journal of Atmospheric and Oceanic Technology **30**, 1398 (2013).
[92] M. B. Wilson, A. L. Houston, C. L. Ziegler, D. M. Stechman, B. Argrow, E. W. Frew, S. Swenson, E. Rasmussen, M. Coniglio, Monthly Weather Review **151**, 3013 (2023).
[93] M. D. Parker, Journal of the Atmospheric Sciences **80**, 1433 (2023).